Fast and stable sampling methods for solving inverse source and scattering problems

by

Thu Thi Anh Le

B.S., Ho Chi Minh City University of Education, Vietnam, 2019

AN ABSTRACT OF A DISSERTATION

submitted in partial fulfillment of the
requirements for the degree

DOCTOR OF PHILOSOPHY

Department of Mathematics
College of Arts and Sciences

KANSAS STATE UNIVERSITY
Manhattan, Kansas

2024

Abstract

This work focuses on fast and stable numerical methods for solving inverse source and scattering problems, utilizing sampling-type methods and deep learning. Our objective is to accurately reconstruct unknown sources or objects using measurements of outgoing waves, focusing on two primary models: acoustic waves governed by Helmholtz equations and electromagnetic waves described by Maxwell's equations.

We first propose a robust and computationally inexpensive sampling-type method for reconstructing small acoustic sources from boundary Cauchy data at a single frequency. This method efficiently identifies the location and intensity of sources, supported by a theoretical foundation using the Green representation formula and an asymptotic expansion for small-volume sources. We validate this approach through 2D numerical examples with synthetic data.

We then expand this technique to address the acoustic inverse scattering problem, applying a versatile imaging function suitable for both near-field and far-field data. We provide a rigorous analysis to establish the decay rate of the imaging function. Integration with a deep neural network featuring a U-net architecture allows us to effectively solve the problem. This combined method accelerates the training process, provides accurate reconstruction, and excels in handling noisy and one incident wave data. Numerical examples in 2D using synthetic data are provided.

Finally, we modify the orthogonality sampling method to accommodate a wider range of polarization vectors associated with data for electromagnetic inverse scattering problems. This method is analyzed using the factorization analysis for the far-field operator and the Funk–Hecke formula. We validate its performance against 3D experimental data from Fresnel, comparing it to both its original formulation and traditional factorization methods.

Numerical studies demonstrate that our method performs better than these approaches on this specific sparse and limited-aperture real dataset in a fast and simple manner.

The results are taken from my published papers[1–3], coauthored with my advisor and our collaborators.

Fast and stable sampling methods for solving inverse source and scattering problems

by

Thu Thi Anh Le

B.S., Ho Chi Minh City University of Education, Vietnam, 2019

A DISSERTATION

submitted in partial fulfillment of the
requirements for the degree

DOCTOR OF PHILOSOPHY

Department of Mathematics
College of Arts and Sciences

KANSAS STATE UNIVERSITY
Manhattan, Kansas

2024

Approved by:

Major Professor
Dinh-Liem Nguyen

Copyright

Abstract

This work focuses on fast and stable numerical methods for solving inverse source and scattering problems, utilizing sampling-type methods and deep learning. Our objective is to accurately reconstruct unknown sources or objects using measurements of outgoing waves, focusing on two primary models: acoustic waves governed by Helmholtz equations and electromagnetic waves described by Maxwell's equations.

We first propose a robust and computationally inexpensive sampling-type method for reconstructing small acoustic sources from boundary Cauchy data at a single frequency. This method efficiently identifies the location and intensity of sources, supported by a theoretical foundation using the Green representation formula and an asymptotic expansion for small-volume sources. We validate this approach through 2D numerical examples with synthetic data.

We then expand this technique to address the acoustic inverse scattering problem, applying a versatile imaging function suitable for both near-field and far-field data. We provide a rigorous analysis to establish the decay rate of the imaging function. Integration with a deep neural network featuring a U-net architecture allows us to effectively solve the problem. This combined method accelerates the training process, provides accurate reconstruction, and excels in handling noisy and one incident wave data. Numerical examples in 2D using synthetic data are provided.

Finally, we modify the orthogonality sampling method to accommodate a wider range of polarization vectors associated with data for electromagnetic inverse scattering problems. This method is analyzed using the factorization analysis for the far-field operator and the Funk–Hecke formula. We validate its performance against 3D experimental data from Fresnel, comparing it to both its original formulation and traditional factorization methods.

Numerical studies demonstrate that our method performs better than these approaches on this specific sparse and limited-aperture real dataset in a fast and simple manner.

The results are taken from my published papers[1–3], coauthored with my advisor and our collaborators.

Table of Contents

List of Figures

Acknowledgments

I would like to express my deepest gratitude to my advisor, Dr. Dinh-Liem Nguyen, for his invaluable guidance, unwavering support, and insightful feedback throughout my PhD journey. His exceptional mentorship has been pivotal to my academic and personal development, providing me with many great opportunities for my career. Dr. Nguyen has been not only a dedicated academic guide, teaching me much about the field, but also a great source of inspiration for growing my passion for research. I feel so lucky to have had him as my advisor. I am also deeply thankful to both Dr. Nguyen and his wife, Diem Huynh, for their willingness to help me from my very first days at K-State. Truly, I could not have embarked on or completed this journey without his profound contributions.

I am incredibly grateful to my committee members, Dr. Bacim Alali, Dr. Behzad Ghanbarian, and Dr. Anna Zemlyanova, not only for their time, consideration, and patience but also for their intellectual contributions and expert guidance. Their involvement is crucial during my qualifying exams and defense, and I really appreciate their thorough review of this dissertation. Their insights have significantly enriched my academic experience and improved the quality of my work.

I want to express my sincere gratitude to the entire Mathematics Department at Kansas State University. Their supportive learning environment, filled with great professors and staff, has been instrumental in my academic journey. Special thanks go to Dr. Marianne Korten, Dr. Pietro Poggi-Corradini, Dr. Nathan Albin, and Dr. Andrew Bennett for their invaluable support, assistance, and guidance. From the professional yet friendly atmosphere to the opportunities for growth, K-State's Math Department has been a crucial stepping stone in my path.

My heartfelt thanks go to my family, my boyfriend, and his family. Their unconditional love, help, and support have been an invaluable source of encouragement, giving me the strength to persevere throughout this process. Words cannot fully convey my appreciation

for the immense role my parents have played in my life. Thank you Mom and Dad for believing in me, giving me the freedom to pursue my passion, and always supporting my decisions.

My heart is filled with happiness and gratitude for the friends and community I have here during my studies. They have made my life less challenging and my journey more enjoyable. A special thank you to my friend Trung, whose advice and support have greatly assisted me professionally. I am deeply grateful for his help and guidance. I also extend my heartfelt thanks to my friends and the Vietnamese community, my roommates, my church community, and my colleagues: Hien, Kamrul, Huong's family, Giang's family, Macie's family, Shumaila, Huynh, Chanh, Nhung, Su, Vi, My, Huy, Thinh, Hannah, Maggie, and many more whom I cannot all include here. I sincerely thank everyone for their warmth, kindness, and support, for their friendship and fellowship. Thanks all for standing by me, sharing with me, and supporting me throughout this journey, thank you from the bottom of my heart.

Chapter 1

Introduction

In this dissertation, we study fast and stable numerical methods for solving inverse source and scattering problems associated with wave equations governed by partial differential equations. The inverse problems aim to reconstruct the physical and/or geometric properties of unknown sources or scatterers using the measurement of outgoing waves. These problems arise naturally and hold critical applications across various areas, including non-destructive testing[4], medical imaging[5;6], geophysical exploration[7], antenna synthesis[8;9], pollution source tracing[10], and military surveillance[11]. The study of these problems has only emerged since the 1980s. Inverse problems have presented considerable challenges for researchers due to their inherent non-linearity and/or severe ill-posedness. In particular, even minor perturbations in the measured data can lead to significant errors in the reconstruction results.

We investigate sampling methods that have garnered significant research interest over the past two decades[12–27]. These numerical methods require less a priori information about scatterers and are less computationally expensive than iterative approaches[28–32]. The Linear Sampling Method (LSM) in[33] and the Factorization Method (FM) in[34] represent the earliest sampling methods, initially applied in acoustic[12] and electromagnetic[13] scattering scenarios. They offer rigorous mathematical analysis and simple computation. However, they require scattering data with multiple incident waves and are sensitive to noise in the datasets. To address this, we developed new sampling methods that provide more stable solutions to

both inverse source and scattering problems. These approaches are flexible in measurement distance and can be applied to data from arbitrary distances. Additionally, we study a combined method that extends a sampling technique and integrates a deep convolutional neural network to effectively solve the inverse problem under one incident wave data. We then validate our methods through comprehensive testing with both simulated and experimental data.

Our methods draw inspiration from the orthogonality sampling method (OSM) proposed by Potthast in[14] for sound-soft acoustic scatterers. This method has attracted attention for its enhanced robustness against noise and its straightforward mathematical justification of stability compared to traditional sampling methods. It was explored for the Helmholtz equation in[15–17] and Maxwell's equations in[18]. However, its theoretical foundation still needs to be developed. This has inspired our research to significantly enhance new sampling techniques' mathematical justification and numerical performance. We also refer to[19–21] for recently developed sampling methods sharing similar features to the OSM. The results in this part are taken from my published paper, coauthored with my advisor and our collaborators.

Below, we outline the motivations for each chapter in the dissertation and summarize their contents.

- In chapter 2, we will focus on solving the acoustic inverse source problem for the Helmholtz equation using Cauchy measurements at a fixed frequency. The problem has been studied by many researchers, although most approaches use data involving multiple frequencies. Solving the problem with a fixed frequency is notably more complex due to its non-uniqueness caused by non-radiation sources. Some iterative studies, such as those found in[28;29], required priori information about the sources to achieve a unique solution. Stability is another challenging issue, as small errors in data can lead to large errors in the reconstruction. We will introduce a sampling-type method with a new imaging function to determine the number of unknown radiating point sources, their locations, and intensities. As mentioned, sampling techniques offer robust computation without initial source knowledge or additional regularization. In contrast to

the direct sampling method in[22], our approach uses a single integral, avoiding multi-level sampling while providing comparably accurate reconstruction results. This offers faster and easier computation, especially for large-scale search domains.

We will provide a theoretical justification of the proposed method using the Green representation formula and the properties of the imaginary part of the Bessel functions, alongside analyzing its stability estimation. Additionally, we will extend the method for small-volume sources by using an asymptotic expansion of the radiated field. Finally, we will present simulated numerical examples in 2D to demonstrate the method's effectiveness.

- In chapter 3, we will consider the acoustic inverse scattering problem for the Helmholtz equation of determining the shape and location of objects from data generated by one incident wave at a fixed frequency. This problem is more challenging than the inverse source problem due to its inherent nonlinearity. It is known that in the case of scattering data generated by one incident wave, the OSM can only provide reasonable reconstructions for small scattering objects[14]. Traditional sampling methods like FM and LSM are ineffective in these cases. This motivates us to combine our sampling-type technique with deep learning to obtain better reconstruction results. The combined method is stable, eliminating the need to train with noise, thus reducing the training information, and preventing overfitting. Additionally, unlike previous methods that required scattering data to be measured on the boundary of a sphere in 3D or a circle in 2D (see[18]), our method allows for the measurement of data on any arbitrary boundary. Several studies, including[35–40], explored and physics-based reconstruction methods to solve inverse problems. However, most of these studies relied on data from multiple incident waves.

  We will extend the sampling-type method in chapter 2, and then combine it with a convolutional neural network to solve the problem under one incident wave data. The resolution analysis of the imaging function will be analyzed where the explicit decay rate of the function will be established. For the deep neural network, we use the U-

Net-Xception style, one of the most recent architectures with extensive applications in computer vision and medical imaging. Training processes and hyperparameter selection will be discussed. This combination leads to a significant improvement in the reconstruction results initially obtained by the sampling method. Numerical studies for simulated data in 2D will be presented.

- In chapter 4, we will address the electromagnetic inverse scattering problem for Maxwell's equations in non-magnetic and magnetic media at a fixed frequency, using 3D experimental data from the Fresnel Institute. There have been results on experimental data verification for sampling methods. Most of these results are for 2D data. The 3D data for two spheres from the Fresnel Institute was studied in [41] with a direct sampling method under a small volume hypothesis of well-separated inhomogeneities. Note that the modified sampling-type method we study does not require this hypothesis. Some other results on inverting these 3D experimental data can be found in [30–32] and references therein. Compared with these results, our method uses only co-polarized (PP) datasets at a single frequency. In addition, the implementation of the OSMs is simpler, faster, and less expensive than those of the iterative methods studied in the cited papers. Note that the method can only recover geometrical information of objects. The main challenge in inverting these 3D real data is that these are sparse data, only the third component of the electric field is measured, and it is measured on a circle. It is shown in the experimental data verification that the proposed method can successfully invert the real data and performs better than its original version and the classical FM.

  We will first investigate a modified version of the OSM in [27] to accommodate a wider range of polarization vectors associated with the scattering data. We will analyze the modified OSM using factorization analysis for the far-field operator and the Funk–Hecke formula. The second goal is to apply the modified OSM, the original OSM, and the classical FM, to the inversion of 3D experimental data. 3D experimental data validation will be provided.

- In chapter 5, we give a summary of the work in this dissertation as well as possible

future work related to this topic.

Chapter 2

Fast Identification of Small Radiating Sources

2.1 Formulation of the acoustic inverse point source problem

In this section, we study a sampling-type method for the inverse source problem of determining radiating point sources from Cauchy data at a fixed frequency for the Helmholtz equation. We consider a set of $N \in \mathbb{N}$ point sources located at $x_j \in \mathbb{R}^d$ for $j = 1, 2, \ldots, N$, and $d = 2$ or 3. These point sources are represented by the Delta distribution δ_{x_j} and have nonzero intensities $\alpha_j \in \mathbb{C}$. In the context of the human brain, these point sources can represent the active channels present within the nerve membrane. Let $k > 0$ be the wave number. Suppose that the sources are well-separated, meaning that $\text{dist}_{i \neq j}(x_i, x_j) \gg \lambda$, where $\lambda = 2\pi/k$ is the wavelength.

We then assume that the sources generate the acoustic radiated field $u : \mathbb{R}^d \to \mathbb{C}$ that

satisfies the following model

$$\Delta u + k^2 u = -\sum_{j=1}^{N} \alpha_j \delta_{x_j}, \quad \text{in } \mathbb{R}^d, \tag{2.1.1}$$

$$\lim_{r\to\infty} r^{\frac{d-1}{2}} \left(\frac{\partial u}{\partial r} - iku \right) = 0, \quad r = |x|, \tag{2.1.2}$$

with the Sommerfeld radiation condition (2.1.2) holds uniformly along all directions $x/|x|$.

It is well-known that the radiated u to (2.1.1)-(2.1.2) can be represented in terms of the free-space Green function

$$u(x) = \sum_{j=1}^{N} \alpha_j \Phi(x, x_j), \quad \text{in } \mathbb{R}^d, \tag{2.1.3}$$

where the Green function $\Phi(x, y)$ is the fundamental solution to the problem (2.1.1)-(2.1.2) and is given by

$$\Phi(x, y) = \begin{cases} \frac{i}{4} H_0^{(1)}(k|x-y|), & \text{in } \mathbb{R}^2, \\ \frac{e^{ik|x-y|}}{4\pi|x-y|}, & \text{in } \mathbb{R}^3, \end{cases} \tag{2.1.4}$$

for any $x \neq y$. Here, $H_0^{(1)}$ is the first kind of Hankel function of order zero.

Let $\Omega \subset \mathbb{R}^d$ be a regular bounded domain with the Lipschitz boundary $\partial\Omega$, where the radiated field is measured. Assume all point sources are within this domain, $x_j \in \Omega$ for $j = 1, 2, \ldots, N$. Denote by $\nu(x)$ the outward normal unit vector to the boundary $\partial\Omega$. We now state the inverse source problem as below.

Inverse problem: Given the Cauchy data of u and $\partial u/\partial\nu$ on the boundary measurement $\partial\Omega$ for a fixed wave number$k$, determine the number of unknown point sources N, their locations x_j and intensities α_j for $j = 1, 2, \ldots, N$.

Note that when dealing with a single wave number k, the Cauchy data is crucial to establish the uniqueness of the solution to this inverse problem (see[10;28]).

2.2 A sampling-type method

We now investigate a sampling-type approach to solve the inverse source problem. The Helmholtz integral representation below is helpful to the analysis of the method.

Lemma 2.2.1. *Assume that W is bounded Lipschitz domain in $\mathbb{R}^d$ such that $\mathbb{R}^d \backslash \overline{W}$ is connected. Let ν be a unit outward normal vector on ∂W. For any function $w \in H^2(W)$, we have*

$$w(x) = \int_{\partial W} \left(\frac{\partial w(y)}{\partial \nu(y)} \Phi(x,y) - w(y) \frac{\partial \Phi(x,y)}{\partial \nu(y)} \right) ds(y) - \int_W (\Delta w + k^2 w) \Phi(x,y) dy. \quad (2.2.1)$$

Proof. We refer to [42, Chapter 2] for a proof of the lemma. □

The next lemma is important for the theoretical justification of the imaging function in the sampling-type method.

Lemma 2.2.2. *The following identity holds for the radiated field u in (2.1.3)*

$$\int_{\partial \Omega} \left(\frac{\partial \mathrm{Im}\, \Phi(x,z)}{\partial \nu(x)} u(x) - \mathrm{Im}\, \Phi(x,z) \frac{\partial u(x)}{\partial \nu(x)} \right) ds(x) = \sum_{j=1}^{N} \alpha_j \mathrm{Im}\, \Phi(x_j, z). \quad (2.2.2)$$

Proof. Substitute the Green representation of u in (2.1.3) to the left hand side of (2.2.2), we have

$$\int_{\partial \Omega} \left(\frac{\partial \mathrm{Im}\, \Phi(x,z)}{\partial \nu(x)} u(x) - \mathrm{Im}\, \Phi(x,z) \frac{\partial u(x)}{\partial \nu(x)} \right) ds(x) \quad (2.2.3)$$

$$= \int_{\partial \Omega} \left(\frac{\partial \mathrm{Im}\, \Phi(x,z)}{\partial \nu(x)} \sum_{j=1}^{N} \alpha_j \Phi(x, x_j) - \mathrm{Im}\, \Phi(x,z) \sum_{j=1}^{N} \alpha_j \frac{\partial \Phi(x, x_j)}{\partial \nu(x)} \right) ds(x) \quad (2.2.4)$$

$$= \sum_{j=1}^{N} \alpha_j \int_{\partial \Omega} \left(\frac{\partial \mathrm{Im}\, \Phi(x,z)}{\partial \nu(x)} \Phi(x, x_j) - \mathrm{Im}\, \Phi(x,z) \frac{\partial \Phi(x, x_j)}{\partial \nu(x)} \right) ds(x). \quad (2.2.5)$$

Given that the imaginary part of the fundamental Green function solution satisfies

$$\Delta \mathrm{Im}\, \Phi(x,y) + k^2 \mathrm{Im}\, \Phi(x,y) = 0,$$

for all $x, y \in \mathbb{R}^d$, and $\operatorname{Im}\Phi(x,y)$ is a regular function, the Helmholtz integral representation in (2.2.1) implies that

$$\int_{\partial\Omega}\left(\frac{\partial \operatorname{Im}\Phi(x,z)}{\partial\nu(x)}\Phi(x,y) - \operatorname{Im}\Phi(x,z)\frac{\partial\Phi(x,y)}{\partial\nu(x)}\right)ds(x) = \operatorname{Im}\Phi(y,z). \tag{2.2.6}$$

This completes the proof. □

We now propose a new imaging function for the recovery of small acoustic radiating sources. Let $z \in \mathbb{R}^d$ be a sampling point, define

$$I(z) := \int_{\partial\Omega}\left(\frac{\partial \operatorname{Im}\Phi(x,z)}{\partial\nu(x)}u(x) - \operatorname{Im}\Phi(x,z)\frac{\partial u(x)}{\partial\nu(x)}\right)ds(x). \tag{2.2.7}$$

Therefore, from Lemma 2.2.2, we obtain that

$$I(z) = \sum_{j=1}^{N}\alpha_j \operatorname{Im}\Phi(x_j,z),$$

where the imaginary part of the Green function is given by

$$\operatorname{Im}\Phi(x,z) = \begin{cases} \frac{1}{4}J_0(k|x-z|), & \text{in } \mathbb{R}^2, \\ \frac{k}{4\pi}j_0(k|x-z|), & \text{in } \mathbb{R}^3, \end{cases} \tag{2.2.8}$$

for any $x, z \in \mathbb{R}^d$. Here, J_0 and j_0 are respectively a Bessel function and a spherical Bessel function of the first kind. In fact, $\operatorname{Im}\Phi(x,z)$ attains its maximum at $z = x$ and decays as z is away from x with

$$J_0(k|x-z|) = \mathcal{O}(|x-z|^{-1/2}) \quad \text{and} \quad j_0(k|x-z|) = \mathcal{O}(|x-z|^{-1}), \qquad \text{as } |x-z| \to \infty.$$

Thus, we can determine N as the number of significant peaks of $|I(z)|^p$, where $p > 0$ is chosen to sharpen the peaks of the imaging function. Then, x_j can be determined as the locations where $|I(z)|^p$ exhibits significant peaks. It follows that the resolution for imaging

the sources is within the diffraction limit

$$|I(z)|^p = \mathcal{O}\left(\text{dist}(z, X)^{\frac{(1-d)p}{2}}\right), \quad \text{as} \quad \text{dist}(z, X) \to \infty,$$

with $X = \{x_j : j = 1, 2, \ldots, N\}$ represents the set of locations.
Additionally, once we obtain estimations for $\mathbf{x}_j$, their corresponding intensities α_j can be computed as below

$$\alpha_j \approx \frac{I(x_j)}{\text{Im}\,\Phi(x_j, x_j)},$$

since under the assumption of well-separated point sources, $\text{Im}\,\Phi(x_j, x_i) \approx 0$ for any $i \neq j$.

This method is robust against the presence of noise in data. In practice, experimental data are always perturbed by noise. We assume the noisy Cauchy measurements denoted by $u_\delta(x)$ and $\partial_\nu u_\delta(x)$ satisfy

$$\|u(x) - u(x)_\delta\|_{L^2(\partial\Omega)} \leq \delta_1 \|u(x)\|_{L^2(\partial\Omega)},$$
$$\|\partial_\nu u(x) - \partial_\nu u_\delta(x)\|_{L^2(\partial\Omega)} \leq \delta_2 \|\partial_\nu u(x)\|_{L^2(\partial\Omega)},$$

for some constants $\delta_1, \delta_2 > 0$ presenting the level of noise. We can derive the following stability estimate.

Theorem 2.2.3. *Denote by $I_\delta(z)$ the imaging function corresponding to the noisy Cauchy data of $I(z)$. Then, for any $z \in \mathbb{R}^d$ and an integer $p > 0$, when $\max(\delta_1, \delta_2) < 1$,*

$$||I(z)|^p - |I_\delta(z)|^p| \leq \max(\delta_1, \delta_2) M,$$

for some constant $M > 0$ independent from δ_1, δ_2 and z.

Proof. By the triangle inequality and the Cauchy-Schwarz inequality, we have

$$\begin{aligned}
|I(z) - I_\delta(z)| &\leq \|u(x) - u_\delta(x)\|_{L^2(\partial\Omega)} \|\partial_\nu \mathrm{Im}\, \Phi(\cdot, x)\|_{L^2(\partial\Omega)} \\
&\quad + \|\partial_\nu u(x) - \partial_\nu u_\delta(x)\|_{L^2(\partial\Omega)} \|\mathrm{Im}\, \Phi(\cdot, x)\|_{L^2(\partial\Omega)} \\
&\leq \delta_1 \|u(x)\|_{L^2(\partial\Omega)} \|\partial_\nu \mathrm{Im}\, \Phi(\cdot, x)\|_{L^2(\partial\Omega)} + \delta_2 \|\partial_\nu u(x)\|_{L^2(\partial\Omega)} \|\mathrm{Im}\, \Phi(\cdot, x)\|_{L^2(\partial\Omega)} \\
&\leq \max(\delta_1, \delta_2) C,
\end{aligned}$$

where $C := \|u(x)\|_{L^2(\partial\Omega)} \|\partial_\nu \mathrm{Im}\, \Phi(\cdot, x)\|_{L^2(\partial\Omega)} + \|\partial_\nu u(x)\|_{L^2(\partial\Omega)} \|\mathrm{Im}\, \Phi(\cdot, x)\|_{L^2(\partial\Omega)} < \infty$.
For a positive integer p, using the triangle inequality, we estimate

$$\begin{aligned}
||I(z)|^p - |I_\delta(z)|^p| &\leq |I(z) - I_\delta(z)| \left| \sum_{j=0}^{p-1} |I_\delta(z)|^j |I(z)|^{p-1-j} \right| \\
&\leq \max(\delta_1, \delta_2) C \sum_{j=0}^{p-1} |I_\delta(z) - I(z) + I(z)|^j |I(z)|^{p-1-j}
\end{aligned}$$

Note that for any two numbers $a, b > 0$, we have

$$(a+b)^p \leq 2^{p-1}(a^p + b^p) \quad \text{for any } p > 1.$$

That leads to

$$\begin{aligned}
||I(z)|^p - |I_\delta(z)|^p| &\leq \max(\delta_1, \delta_2) C \sum_{j=0}^{p-1} 2^{j-1} \left(|I_\delta(z) - I(z)|^j + |I(z)|^j \right) |I(z)|^{p-1-j} \\
&\leq \max(\delta_1, \delta_2) C \sum_{j=0}^{p-1} 2^{j-1} \left(\max(\delta_1, \delta_2)^j C^j |I(z)|^{p-1-j} + |I(z)|^{p-1} \right).
\end{aligned}$$

In addition, we can show that $|I(z)| \leq C$. Hence,

$$||I(z)|^p - |I_\delta(z)|^p| \leq \max(\delta_1, \delta_2) C \sum_{j=0}^{p-1} 2^{j-1} \left(\max(\delta_1, \delta_2)^j + 1 \right) C^{p-1}$$
$$= \max(\delta_1, \delta_2) C^p \left(2^{p-1} - 1 + \sum_{j=0}^{p-1} 2^{j-1} \max(\delta_1, \delta_2)^j \right).$$

When $\max(\delta_1, \delta_2) < 1$, we get

$$||I(z)|^p - |I_\delta(z)|^p| \leq \max(\delta_1, \delta_2) C^p \left(2^{p-1} - 1 + \sum_{j=0}^{p-1} 2^{j-1} \right) = \max(\delta_1, \delta_2) M,$$

with $M = C^p(2^p - 3/2) > 0$ independent from δ_1, δ_2 and z. □

2.3 Reconstruction of small volume sources

We let D with Lipschitz boundary ∂D have a small volume in $\mathbb{R}^d$ such that $|D| = \mathcal{O}(\epsilon^d)$. To this end, we assume that the small volume source D is given by a collection of small volume subregions

$$D = \cup_{j=1}^N D_j \qquad \text{with } D_j = x_j + \epsilon B_j \quad \text{such that } \operatorname{dist}(x_j, x_i) \gg \lambda,$$

for $i \neq j$. The parameter ϵ is sufficiently small, satisfying $0 < \epsilon \ll 1$. Here, B_j is a bounded, radially symmetric domain with a Lipschitz boundary centered at the origin, and $|B_j| = \mathcal{O}(1)$ for $j = 1, 2, \ldots, N$. The points x_j are assumed to be within Ω. We also suppose that D_j are pairwise disjoint such that $D_j \cap D_i = \emptyset$ for $i \neq j$. Let the source $f \in L^2(D)$ and $\mathbf{1}_D$ be the indicator function on the set D. We assume that the radiated field $u \in H^1_{loc}(\mathbb{R}^d)$ generated by these small sources satisfies

$$\Delta u + k^2 u = -f \mathbf{1}_D, \tag{2.3.1}$$

along with the Sommerfeld radiation condition in (2.1.2).

It is well-known that the radiated field of this problem can be written as the following integral form

$$u(x) = \int_D f(y)\Phi(x,y)dy, \tag{2.3.2}$$

where $\Phi(x,y)$ is the free-space Green function as given in (3.2.2).

Now, we consider the inverse source problem of determining the number of unknown small sources N and center x_j in each subregion for $j = 1, 2, \ldots, N$, from the Cauchy data measurements of u and $\partial_\nu u$ on the boundary $\partial\Omega$.

We have that for any $x \in \mathbb{R}^d \backslash \overline{D}$, we can use a first-order Taylor expansion of the Green function to approximate the radiated field u. Therefore, we notice that $y \in D_j$ if and only if $y = x_j + \epsilon\omega$ for some $\omega \in B_j$ which gives us that

$$\begin{aligned} u(x) &= \int_D f(y)\Phi(x,y)dy \\ &= \sum_{j=1}^{N} \int_{D_j} f(y)\Phi(x, x_j + \epsilon\omega)dy \\ &= \sum_{j=1}^{N} \left(\Phi(x,x_j) + \mathcal{O}(\epsilon)\right) \int_{D_j} f(y)dy. \end{aligned}$$

Let $\overline{f}_{D_j}$ denote the average value of f on the subregion D_j. In other words,

$$\overline{f}_{D_j} = \frac{1}{|D_j|} \int_{D_j} f(y)\,\mathrm{d}y \quad \text{for all} \quad j = 1, 2, \ldots, N.$$

And by using the fact that $|D_j| = \epsilon^d |B_j|$, we obtain that

$$u(x) = \epsilon^d \sum_{j=1}^{N} \overline{f}_{D_j} |B_j| \Phi(x, x_j) + \mathcal{O}(\epsilon^{d+1}). \tag{2.3.3}$$

This gives that, up to leading order, u acts like a radiated field generated by point sources located at x_j with intensity $\alpha_j = \epsilon^d \overline{f}_{D_j} |B_j|$. Again, by using the representation in (2.3.3)

and the Green formula for $\operatorname{Im}\Phi(x,z)$, we derive that

$$\int_{\partial\Omega}\left(\frac{\partial \operatorname{Im}\Phi(x,z)}{\partial\nu(x)}u(x)-\operatorname{Im}\Phi(x,z)\frac{\partial u(x)}{\partial\nu(x)}\right)ds(x)=\epsilon^d\sum_{j=1}^{N}\overline{f}_{D_j}|B_j|\operatorname{Im}\Phi(x_j,z)+\mathcal{O}(\epsilon^{d+1}). \tag{2.3.4}$$

As in the case of point sources, this identity allows us to use the proposed imaging function $I(z)$ defined (2.2.7) to determine centers x_j of small volume sources. Specifically, they can be determined as the locations where $|I(z)|^p$ has significant peaks. Moreover, up to the leading order, if $\overline{f}_{D_j}\neq 0$ we have that for all $z\in\mathbb{R}^d\backslash\overline{D}$

$$|I(z)|^p=\mathcal{O}\left(\operatorname{dist}(z,X)^{\frac{(1-d)p}{2}}\right),\quad \text{as}\quad \operatorname{dist}(z,X)\to\infty,$$

with the set $X=\{x_j : j=1,2,\dots,N\}$.

2.4 Numerical results

We now present numerical results for the new sampling-type method to identify small sources in two dimensions. In all of the numerical examples, the wave number is chosen as $k=20$ and the Cauchy data is given at 256 points which are uniformly distributed on the circle centered at the origin with a radius of 50 (which is about 159 wavelengths). The synthesis data is computed in MATLAB using (2.1.3) and (2.3.2), respectively with 10% random noise added to the data. The noise vectors $\mathcal{N}_{1,2}$ consist of numbers $a+ib$ where $a,b\in(-1,1)$ are randomly generated with a uniform distribution. We consider the same noise level for both u and $\partial_\nu u$ for simplicity. The noise vectors are added to u and $\partial_\nu u$ as follows

$$u+10\%\frac{\mathcal{N}_1}{\|\mathcal{N}_1\|_F}\|u\|_F\quad \partial_\nu u+10\%\frac{\mathcal{N}_2}{\|\mathcal{N}_2\|_F}\|\partial_\nu u\|_F,$$

where $\|\cdot\|_F$ is the Frobenius matrix norm. The imaging function $I(z)$ is computed at 256×256 uniformly distributed sampling points on the search domain $[-2,2]^2$. That means the

distance between two consecutive sampling points is about 0.05 wavelength. This distance is small enough since the sources are supposed to be well-separated.

The reconstruction results for the location and intensity of different numbers of point sources can be seen in Table 2.1 and Figure 2.1. The number of significant peaks of $|I(z)|^p$ with $p = 4$ is clearly shown in Figure 2.1. We determine the number of sources N and x_j for $j = 1, 2, \ldots, N$ as the location of these peaks. Table 2.1 shows that the locations x_j of the point sources are computed with high accuracy. Additionally, the intensities α_j are recovered with reasonable relative errors, ranging from 1% to 10%. In particular, the method can reasonably compute the location and intensity of two point sources located within a close distance of a wavelength. It is noticed that the error gets worse as the number of sources to compute increases.

We display in Table 2.2 and Figure 2.2 the reconstruction results of sources that are small disks. The centers x_j of these circular sources are again computed with very good accuracy. It is worth noting that the magnitudes of source intensities considered in this section are not significantly different from each other. If there is a large discrepancy in the magnitudes of the source intensities, the method may not be able to determine the sources with smaller intensities. This drawback, also highlighted in[22], remains an open question that inspires our future research.

N	True location	Computed location	True intensity	Computed intensity
2 (close)	$(0.15, 0)$,	$(0.125, 0.000)$,	$1 - 2i$,	$0.942 - 1.881i$,
	$(-0.15, 0)$	$(-0.125, 0.000)$	$1 + 2i$	$0.950 + 1.899i$
2 (distant)	$(-1, 0.8)$,	$(-1.000, 0.796)$,	$1 - 2i$,	$1.007 - 2.045i$,
	$(0.7, -1)$	$(0.703, -1.000)$	$1 + 2i$	$1.024 + 2.004i$
3	$(1, -1)$,	$(1.000, -0.984)$,	4,	$3.912 + 0.023i$,
	$(1.3, 1)$,	$(1.312, 0.984)$,	$3.5 - i$,	$3.431 - 0.918i$,
	$(-1.2, -0.25)$	$(-1.203, -0.250)$	$3.5 + i$	$3.570 + 0.968i$
4	$(1, -1)$,	$(1.015, -1.000)$,	$2.5 + 2i$,	$2.725 + 2.237i$,
	$(1, 0.75)$,	$(1.015, 0.750)$,	$2.5 - 2i$,	$2.759 - 2.158i$,
	$(-1.2, -1)$,	$(-1.203, -1.000)$,	$3.5 - i$,	$3.532 - 1.035i$,
	$(-1.2, 0.75)$	$(-1.203, 0.750)$	$3 + i$	$2.982 + 1.077i$

Table 2.1: Reconstruction results for the location and intensity of point sources.

N	True location	Computed location
3	$(1, 0.75), (-1, -1), (1.25, -1.5)$	$(0.984, 0.734), (-0.984, -1.000), (1.234, -1.500)$
4	$(1, 1), (-1, -1.25),$	$(0.984, 0.984), (-0.984, -1.234),$
	$(1, -1), (-1, 0.75)$	$(0.984, -0.984), (-0.984, 0.734)$
5	$(1.25, 1.2), (-1, 0), (1, -1),$	$(1.265, 1.203), (-1.000, 0.015), (1.000, -1.015),$
	$(-0.6, 1), (0.25, 0)$	$(-0.609, 0.984), (0.250, 0.000)$

Table 2.2: Reconstruction results for the center of small disks.

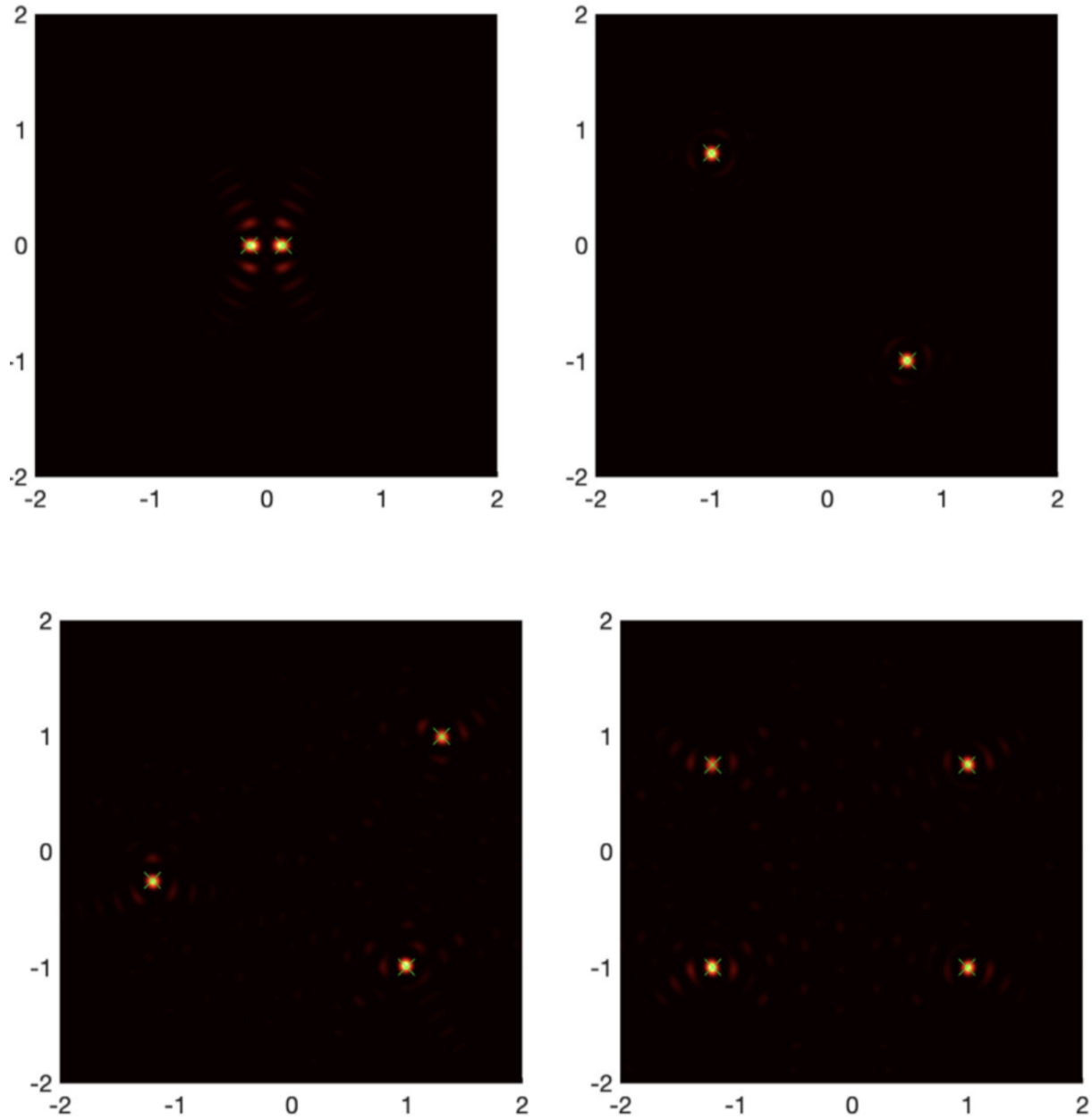

Figure 2.1: Pictures of $|I(z)|^4$ for point sources. The true locations of the sources are displayed by the green crosses.

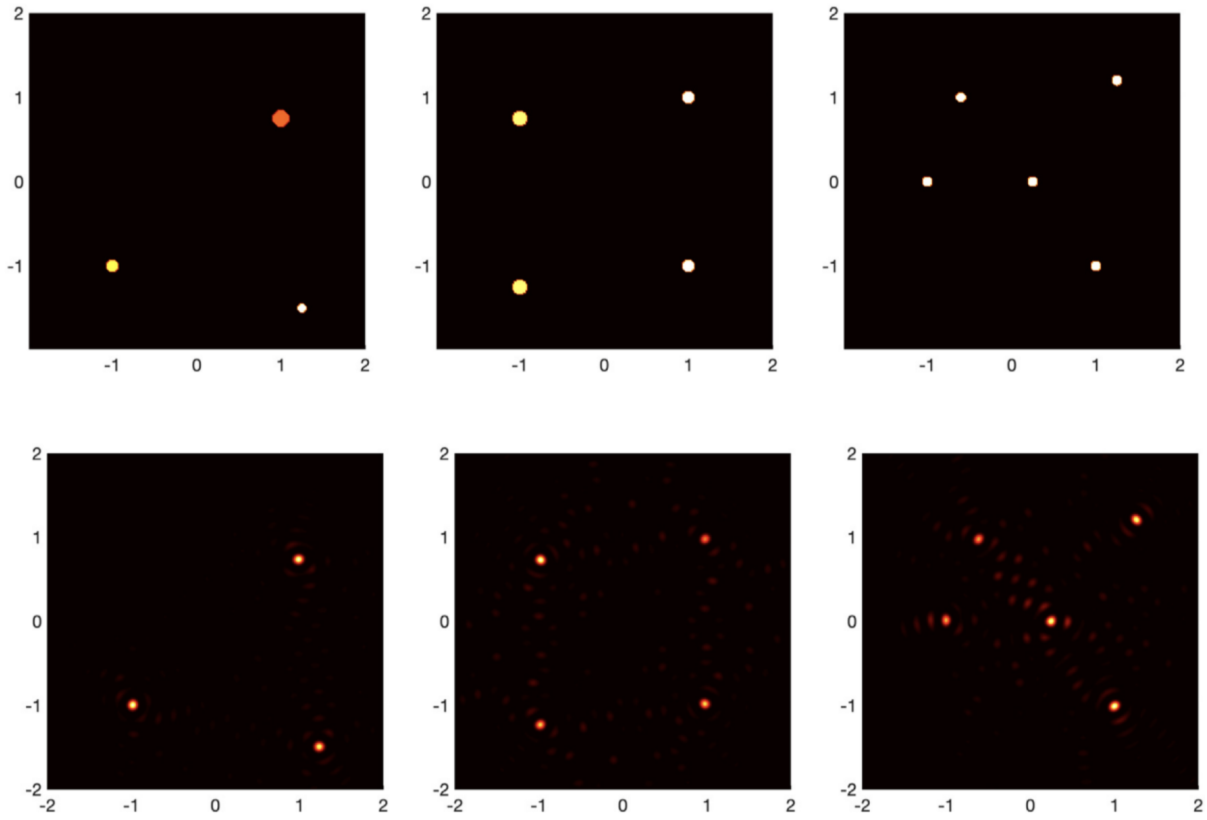

Figure 2.2: The first row is the true profile of small volume sources (the color of the disks is associated with the value of f on each disk that we are not able to recover using $I(z)$). The second row contains pictures of $|I(z)|^4$.

Chapter 3

Deep Learning Enhanced Imaging of Scattering Objects from Limited Data

3.1 Formulation of the acoustic inverse scattering problem

In this section, we focus on solving the inverse scattering problem for acoustic waves related to the Helmholtz equation, which aims to recover the shape and location of a scattering object from limited measurement data. We consider a penetrable inhomogeneous bounded medium with Lipschitz domain denoted as D, characterized by a bounded index of refraction function $\eta(x) : \mathbb{R}^d \to \mathbb{C}$ satisfying $\eta = 0$ in $\mathbb{R}^d \backslash D$, with $d = 2$ or 3. In our setup, an incident wave, modeled as a time-harmonic acoustic plane wave $u^{in}(x) = e^{ikx\cdot d_{in}}$, illuminates the medium. Here, $k > 0$ is the wave number, and $d_{in} \in \mathbb{R}^d$ is the direction of wave propagation. Denote the total wave by $u : \mathbb{R}^d \to \mathbb{C}$. Then, there arises the scattered acoustic wave $u^{sc} := u - u^{in}$. The following model describes the scattering phenomenon

$$\Delta u + k^2 \left[1 + \eta(x)\right] u = 0, \quad \text{in } \mathbb{R}^d, \tag{3.1.1}$$

$$\lim_{r\to\infty} r^{\frac{n-1}{2}} \left(\frac{\partial u^{sc}}{\partial r} - iku^{sc} \right) = 0, \quad r = |x|, \tag{3.1.2}$$

with the Sommerfeld radiation condition (3.1.2) holds uniformly for all directions $x/|x|$ in $\mathbb{S}^{d-1} := \{x \in \mathbb{R}^d : |x| = 1\}$.

If $\mathbb{R}^d \backslash \overline{D}$ is connected and $\operatorname{Re} \eta \geq 0$, this scattering problem is known to have a unique weak solution $u^{sc} \in H^1_{loc}(\mathbb{R}^d)$, see[42]. Let Ω be a bounded Lipschitz domain such that $\overline{D} \subset \Omega$ and denote by $\nu(x)$ the outward normal unit vector to $\partial\Omega$ at x. Below is the inverse scattering problem with one incident wave data that we are interested in solving

Inverse problem: Given the Cauchy data of u_{sc} and $\partial u_{sc}/\partial\nu$ on the boundary measurement $\partial\Omega$ from a single incident wave and at a fixed wave number k, determine the domain D.

3.2 A sampling-type method

We now explore a sampling-type technique and integrate it with deep learning to solve this problem. Similarly, the free-space Green function of the scattering problem (3.1.1)-(3.1.2) is $\Phi(x, y)$ as defined in (2.1.3).

It is well-known that problem (3.1.1)-(3.1.2) is equivalent to the Lippmann-Schwinger equation (see,[42])

$$u_{sc}(x) = k^2 \int_D \Phi(x, y)\eta(y)u(y)dy, \quad x \in \mathbb{R}^d.$$

We need to use the following Funk-Hecke formula to analyze the sampling method in this section.

Lemma 3.2.1. *Let Y_m be the spherical harmonics of order m and j_m be the spherical Bessel functions of the first kind and order m. We have*

$$\int_{\mathbb{S}^{d-1}} e^{-ikx\cdot z} Y_n(z)ds(z) = \frac{4\pi}{i^m} j^m(k|x|)Y_m\left(\frac{x}{|x|}\right).$$

Proof. A proof of this lemma can be found in [[42], Chapter 2]. □

Motivated by the definition of the imaging function for the inverse source problem in (2.2.7), we introduce the imaging function for this inverse scattering problem. Let $z \in \mathbb{R}^d$

be a sampling point, define

$$I(z) := \left| \int_{\partial\Omega} \left(\frac{\partial \mathrm{Im}\, \Phi(x,z)}{\partial \nu(x)} u_{sc}(x) - \mathrm{Im}\, \Phi(x,z) \frac{\partial u_{sc}(x)}{\partial \nu(x)} \right) ds(x) \right|^{\rho} \tag{3.2.1}$$

where $\rho = 1$ or $\rho = 2$.

This function $I(z)$ is designed to identify the domain D within Ω. We expect that $I(z)$ is relatively large when z is within the object D and small as z is away from D. The behavior of the imaging function is analyzed in the following theorem.

Theorem 3.2.2. *The imaging function satisfies*

$$I(z) = \left| k^2 \int_D \mathrm{Im}\, \Phi(y,z) \eta(y) u(y) dy \right|^{\rho}.$$

Proof. From the Lippmann-Schwinger equation, we obtain that

$$\frac{\partial u_{sc}(x)}{\partial \nu(x)} = k^2 \int_D \frac{\partial \Phi(x,y)}{\partial \nu(x)} \eta(y) u(y) dy.$$

Substituting these integral representations into the definition in (3.2.1)

$$\begin{aligned}
&\left| \int_{\partial\Omega} \left(\frac{\partial \mathrm{Im}\, \Phi(x,z)}{\partial \nu(x)} u_{sc}(x) - \mathrm{Im}\, \Phi(x,z) \frac{\partial u_{sc}(x)}{\partial \nu(x)} \right) ds(x) \right|^{\rho} \\
&= \left| \int_{\partial\Omega} \left(\frac{\partial \mathrm{Im}\, \Phi(x,z)}{\partial \nu(x)} k^2 \int_D \Phi(x,y) \eta(y) u(y) dy - \mathrm{Im}\, \Phi(x,z) k^2 \int_D \frac{\partial \Phi(x,y)}{\partial \nu(x)} \eta(y) u(y) dy \right) ds(x) \right|^{\rho} \\
&= \left| k^2 \int_D \int_{\partial\Omega} \frac{\partial \mathrm{Im}\, \Phi(x,z)}{\partial \nu(x)} \Phi(x,y) - \mathrm{Im}\, \Phi(x,z) \frac{\partial \Phi(x,y)}{\partial \nu(x)} ds(x) \eta(y) u(y) dy \right|^{\rho}.
\end{aligned}$$

Now, using the identity of the Green function in (2.2.6) gives

$$\begin{aligned}
I(z) &= \left| \int_{\partial\Omega} \left(\frac{\partial \mathrm{Im}\, \Phi(x,z)}{\partial \nu(x)} u_{sc}(x) - \mathrm{Im}\, \Phi(x,z) \frac{\partial u_{sc}(x)}{\partial \nu(x)} \right) ds(x) \right|^{\rho} \\
&= \left| k^2 \int_D \mathrm{Im}\, \Phi(y,z) \eta(y) u(y) dy \right|^{\rho}.
\end{aligned}$$

□

We know that

$$\operatorname{Im}\Phi(y,z) = \begin{cases} \frac{1}{4}J_0(k|y-z|), & \text{in } \mathbb{R}^2, \\ \frac{k}{4\pi}j_0(k|y-z|), & \text{in } \mathbb{R}^3, \end{cases} \tag{3.2.2}$$

for any $y, z \in \mathbb{R}^d$. Here, J_0 and j_0 are respectively a Bessel function and a spherical Bessel function of the first kind. In fact, $\operatorname{Im}\Phi(y,z)$ peaks at $z = y$ and decays as z is away from y with

$$J_0(k|y-z|) = \mathcal{O}(|y-z|^{-1/2}) \quad \text{and} \quad j_0(k|y-z|) = \mathcal{O}(|y-z|^{-1}), \qquad \text{as } |y-z| \to \infty.$$

Therefore, we expect from Theorem 3.2.2 that $I(z)$ takes larger values for $z \in D$ and much smaller values outside D, up to the leading order

$$I(z) = \mathcal{O}\left(\frac{1}{\operatorname{dist}(z,D)^{\rho(d-1)/2}}\right), \qquad \text{as } \operatorname{dist}(z,D) \to \infty.$$

This incomplete analysis is common for imaging functions of sampling-type methods (see[14–16;43–45]). To our knowledge, a complete analysis of sampling-type methods is still an open problem.

We now show a relation between $I(z)$ and the imaging function suggested by Potthast in[14]. To this end, we recall that the scattered field u_{sc} has the asymptotic behavior

$$u_{sc}(x) = \frac{e^{ik|x|}}{|x|^{d-1/2}}\left(u^\infty(\hat{x}) + \mathcal{O}\left(1/|x|\right)\right), \qquad \text{as } |x| \to \infty,$$

for all $\hat{x} \in \mathbb{S}^{d-1}$. The function $u^\infty(\hat{x})$ is called the scattering amplitude or the far-field pattern of $u_{sc}(x)$. The imaging function of the orthogonality sampling method suggested in[14] is given by

$$I_{OSM}(z) = \left| \int_{\mathbb{S}^{d-1}} e^{ikz\cdot\hat{x}} u^\infty(\hat{x}) ds(\hat{x}) \right|.$$

Theorem 3.2.3. *The two imaging functions are related by*

$$I(z) = \gamma |I_{OSM}(z)|^{\rho},$$

$$\textit{where } \gamma = \begin{cases} \left(\frac{\sqrt{\pi} e^{i\pi/4}}{\sqrt{2k}}\right)^{\rho}, & \textit{in } \mathbb{R}^2, \\ \left(\frac{4\pi}{k}\right)^{\rho}, & \textit{in } \mathbb{R}^3. \end{cases}.$$

Proof. From the Lippmann-Schwinger equation for u_{sc} it is known that its scattering amplitude is given by

$$u^{\infty}(\hat{x}) = \alpha k^2 \int_D e^{-iky\cdot\hat{x}} \eta(y) u(y) dy,$$

$$\text{with } \alpha = \begin{cases} \frac{e^{i\pi/4}}{\sqrt{8\pi k}}, & \text{in } \mathbb{R}^2, \\ \frac{1}{4\pi}, & \text{in } \mathbb{R}^3. \end{cases}$$

Substituting u^{∞} in $I_{OSM}(z)$ implies

$$I_{OSM}(z) = \left| \alpha k^2 \int_D \int_{\mathbb{S}^{d-1}} e^{ik\hat{x}\cdot(z-y)} \eta(y) u(y) ds(\hat{x}) dy \right|. \tag{3.2.3}$$

Using the Funk-Hecke formula in Lemma 3.2.1, we obtain that

$$\int_{\mathbb{S}^{d-1}} e^{ik\hat{x}\cdot(z-y)} ds(\hat{x}) = \begin{cases} 2\pi \text{Im}\, \Phi(z,y), & \text{in } \mathbb{R}^2, \\ \frac{(4\pi)^2}{k} \text{Im}\, \Phi(z,y), & \text{in } \mathbb{R}^3. \end{cases} \tag{3.2.4}$$

Substituting (3.2.4) in (3.2.3) and comparing with Theorem (3.2.2), we complete the proof. □

This Theorem also implies that $I(z)$ is stable against noise in the data, following the stability of $I_{OSM}(z)$ as demonstrated in[14].

Remark 3.2.4. If $\partial\Omega$ is the boundary of some ball with a large radius, we can approximate $\partial_{\nu} u_{sc} \approx iku_{sc}$ using the radiation condition. Then $I(z)$ can be modified to handle the far-field

data $u_{sc}(x)$ as follows

$$I(z) = \left| \int_{\partial\Omega} \left(\frac{\partial \text{Im}\, \Phi(x,z)}{\partial \nu(x)} u_{sc}(x) - ik \text{Im}\, \Phi(x,z) u_{sc}(x) \right) ds(x) \right|^{\rho}.$$

3.3 The deep neural network

We now use the sampling-type method along with a deep neural network of U-Net-Xception style to form a combined method to solve the inverse scattering problem under one wave incident data. Numerical simulation was done for both simulated and experimental scattering data.

3.3.1 U-Net Xception style

Xception is an efficient architecture that relies on two main points: Depthwise Separable Convolution and Shortcuts between Convolution blocks. Xception architecture is an alternative to classical convolution layers, which performs more efficiently in terms of computation time and accuracy. See details of Xception architecture in[46].

Firstly, Depthwise Separable Convolution includes two subnetworks: Depthwise Convolution and Pointwise Convolution. Compared to conventional convolution layers, Depthwise Separable Convolution does not need to compute convolution operations across all channels, which will eliminate the number of parameters in the model and makes it simpler.

Secondly, there are residual (shortcut/skip) connections in Xception networks. Many state-of-the-art Deep neural networks (Resnet, YOLOv3, MobileNetV2, Cascading Residual Network) have shown that accuracy is much higher when residual connections are used, see[47–49].

3.3.2 Training the network

The training data set includes $60,000$ pairs of images, each pair consists of a true image and a preliminary image. A true image represents a scattering object. We illuminate this

object with an incident plane wave from one direction and apply the spectral method in[50] to solve the direct problem, producing the associated scattering data. Using the proposed sampling-type technique on this scattering data, we generate a computed image, referred to as a preliminary image.

The true images are those of either one or two ellipses whose center and radii are randomly generated using a uniform distribution within the square domain $[-2,2]^2$. More precisely, if the object consists of only one ellipse, its center is uniformly distributed within the square $[-0.8,0.8]^2$, and its radii are uniformly distributed within the interval $[0.1,1]$. If the object consists of two ellipses, the first one is generated in the same manner as before, while the second one has its center uniformly generated within the square $[-1,1]^2$, and radii are uniformly distributed within the interval $[0.1,0.5]$. Note that the two ellipses are allowed to overlap each other.

The wave number is chosen to be $k=6$, which means the wavelength is about 1. As for the incident wave, we use

$$u_{in}(x) = e^{ik(x_1\cos\theta + x_2\sin\theta)},$$

where $\theta = 90^o$ for $30,000$ images and $\theta = 45^o$ for the other $30,000$ images. The Cauchy scattering data are computed on the circle of radius 100. We did not add any artificial noise to the scattering data for the training and testing of the network. See Figure 3.1 for examples of training data pairs.

All images are uniformly partitioned into 160×160 pixels. Define $J=\{1,2,\ldots,160^2\}$ to enumerate the pixel order within an image. The neural network is initialized with random parameters. Using a preliminary image as input, the network produces the corresponding output image $\hat{y}=\{\hat{y}_i\}_{i\in J}$ that will then be used along with the true image $y=\{y_i\}_{i\in J}$ to calculate the loss function for individual training pairs

$$L = -\sum_{i\in J}(y_i\log\hat{y}_i + (1-y_i)\log(1-\hat{y}_i)),$$

The overall loss function is the average of this loss across a specified number of samples.

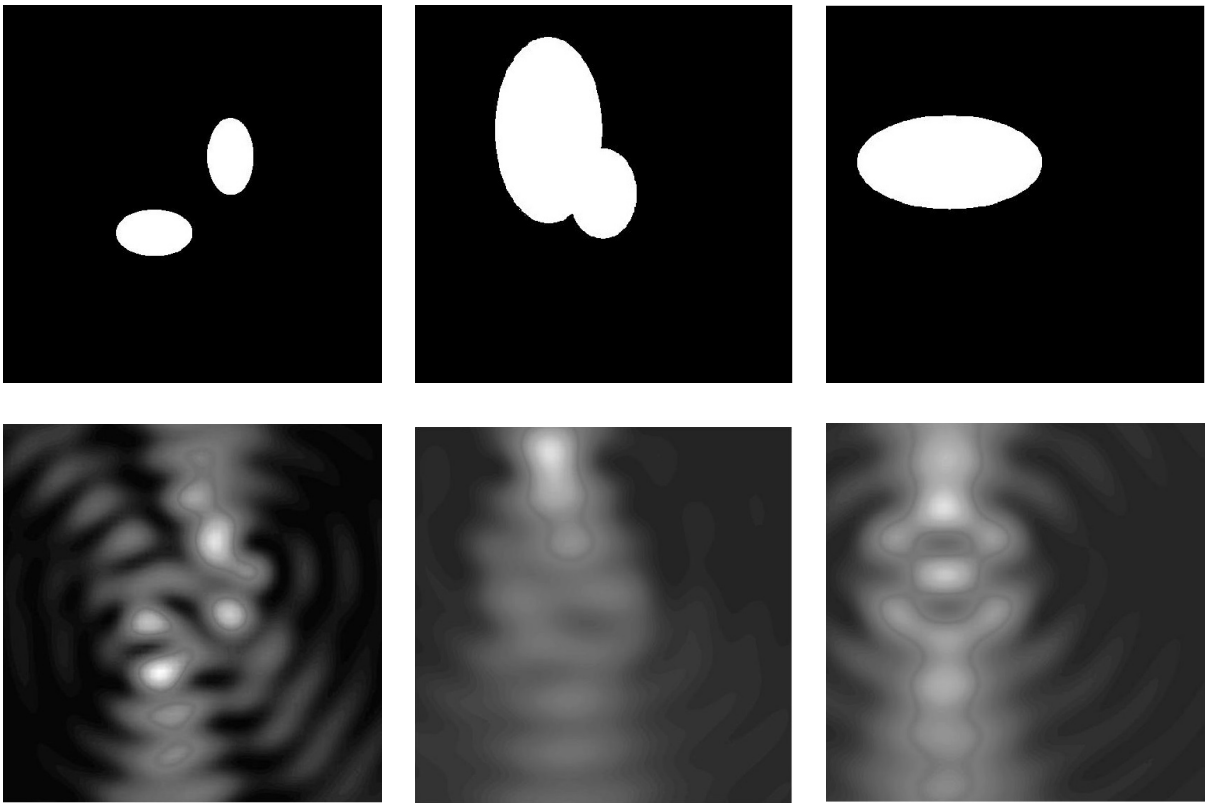

Figure 3.1: Examples of three training data pairs: true images (top), preliminary images (bottom).

After that, the parameters within the convolution layers are tuned using the Adam method to minimize the cost function. This minimization process is done for one batch of size 32 at a time. The initial learning rate is 10^{-2}, and will be divided by 10 if the validation loss does not decrease or validation accuracy does not increase after 5 epochs until it reaches 10^{-6}. The neural network's architecture can be briefly described by the diagram in Figure 3.2.

Out of $60,000$ pairs of images, $50,000$ were used to train the network, $5,000$ were used for validation and $5,000$ were used for testing. In Figure 3.3, we show the result of training loss versus validation loss and training accuracy versus validation accuracy. The loss value at each epoch is the average value of L over all paired images, whereas the accuracy value is the ratio of the number of pixels in the predicted image that match their counterparts in the true image to the total number of pixels. Those values for validation were computed over $5,000$ images in the validation set, and those values for training were computed over $50,000$ images in the training set.

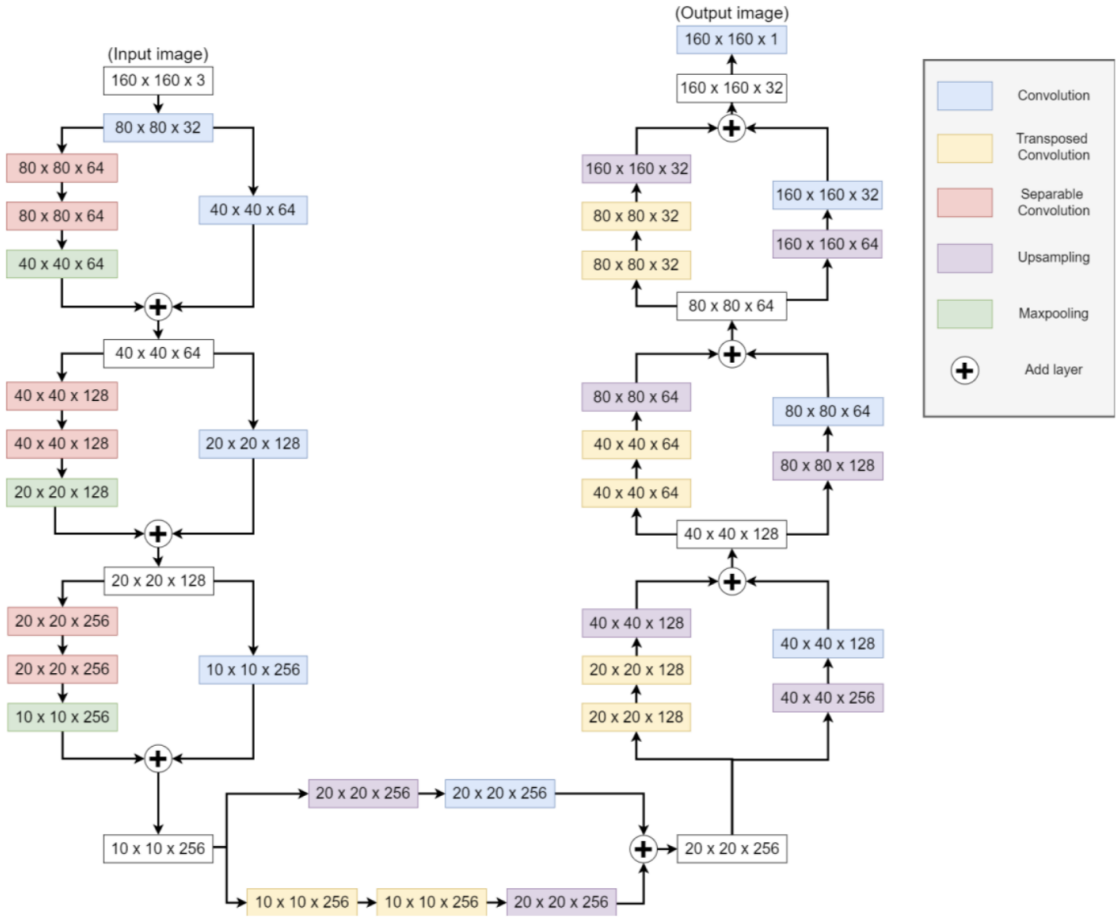

Figure 3.2: Architecture of the neural network.

To enrich the training data set, we used data augmentation. More specifically, we produced five copies of each training pair by applying five types of transformations: horizontal flip, vertical flip, 90^o rotation, and -90^o rotation.

Our choice for some hyperparameters was based on a direct comparison to other choices in terms of validation loss and accuracy. For example, we trained the model with $10,000$ pairs of images through 5 epochs with different input image sizes, then we chose $160 \times 160 \times 3$ because it gave the best values for loss and accuracy. We did a similar experiment for two different optimization methods, which are Adam method and stochastic gradient descent with momentum (SGD), and Adam method performed better for this problem. Detailed results for the comparisons are given in Tables 3.1 and 3.2. As for the other hyperparameters such as the number of hidden layers and units, we followed the same choice as in[46]. With this

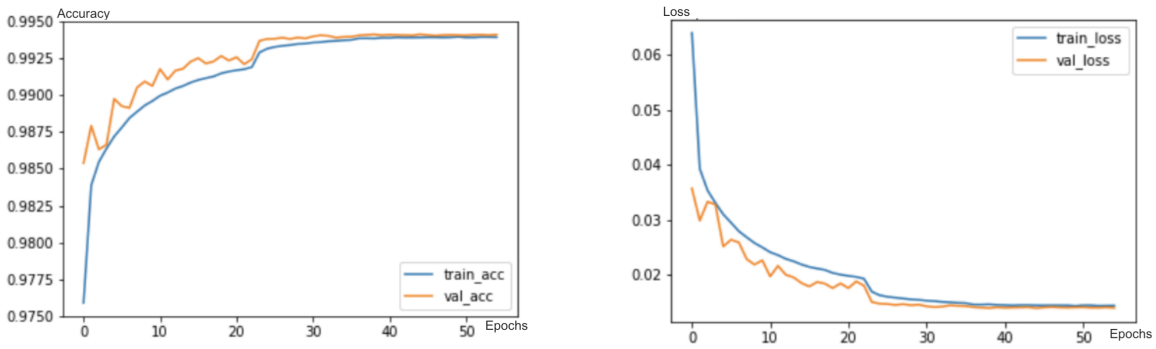

(a) Accuracy (b) Loss

Figure 3.3: Training and validation results after each training iteration over 50 epochs.

choice, we were able to get very good loss and accuracy values, see Figure 3.3. Therefore, no adjustment was needed.

Input image size	Validation accuracy	Validation loss
$32 \times 32 \times 3$	0.9718	0.0677
$64 \times 64 \times 3$	0.9762	0.0579
$128 \times 128 \times 3$	0.9728	0.0713
$\mathbf{160 \times 160 \times 3}$	**0.9822**	**0.0452**
$192 \times 192 \times 3$	0.9749	0.0708

Table 3.1: Input image size comparison.

Optimization method	Validation accuracy	Validation loss
SGD	0.9751	0.0622
Adam	**0.9822**	**0.0452**

Table 3.2: Optimization method comparison.

We also compared the performance of the U-Net Xception style with a modified U-Net. The result in Table 3.3 shows that the U-Net Xception style works better for our problem.

Model	Validation accuracy	Validation loss
Modified U-Net	0.9876	0.0299
U-Net Xception style	**0.9932**	**0.0175**

Table 3.3: Model comparison.

3.4 Numerical results

In this section, we use the combined method to reconstruct objects from simulated scattering data. We consider the types of objects varying from those similar to the training data set to those entirely different. We also tested different wave numbers and incident wave directions.

3.4.1 Implementation of the sampling method

In our numerical study, the sampling domain is chosen as $[-2, 2]^2$. The sampling domain contains the unknown scatterer D and is uniformly discretized by 64 sampling points in each direction. The imaging function $I(z)$ in (3.2.1) is evaluated at each sampling point z of the sampling domain. As mentioned in the section on training the neural network, the data $(u_{sc}, \partial_\nu u_{sc})$ are given at 32 uniformly distributed points on the circle of radius 100. With the data given, the evaluation of $I(z)$ is simple since after a change of variables using polar coordinates, we numerically evaluate a single integral using the rectangular rule. In the numerical simulation, the imaging function is normalized by dividing by its maximal value. Note that we ensure that the sampling point z and the data point x are away from each other so that the integrands are all regular functions. Recall that the scattering data are measured on $\partial\Omega$, meaning that we should look for the unknown scatterer D in a sampling domain that is strictly contained in Ω.

3.4.2 Reconstruction of objects in the testing data set

In this part, we present the reconstruction results of the combined method for objects in the testing data set. These objects were generated in a way that is similar to that of the training data sets, meaning the objects consist of one or two ellipses. The wave number k and incident direction θ were those the neural network was trained with. Moreover, the scattering data generated by solving the direct problem was not perturbed by noise.

In Figures 3.4-3.5, four test objects are presented: one large disk, two ellipses of similar sizes, two ellipses of different sizes, and two overlapping ellipses. We can see that the method

was able to reconstruct very well the geometry of these test objects. As it was done for the validation and training data sets in Figure 3.3, the accuracy for 5000 pairs of images in the testing data set is also computed as 99.4%. This once again confirms that the training process was effective as indicated by the training and validation accuracy in Figure 3.3.

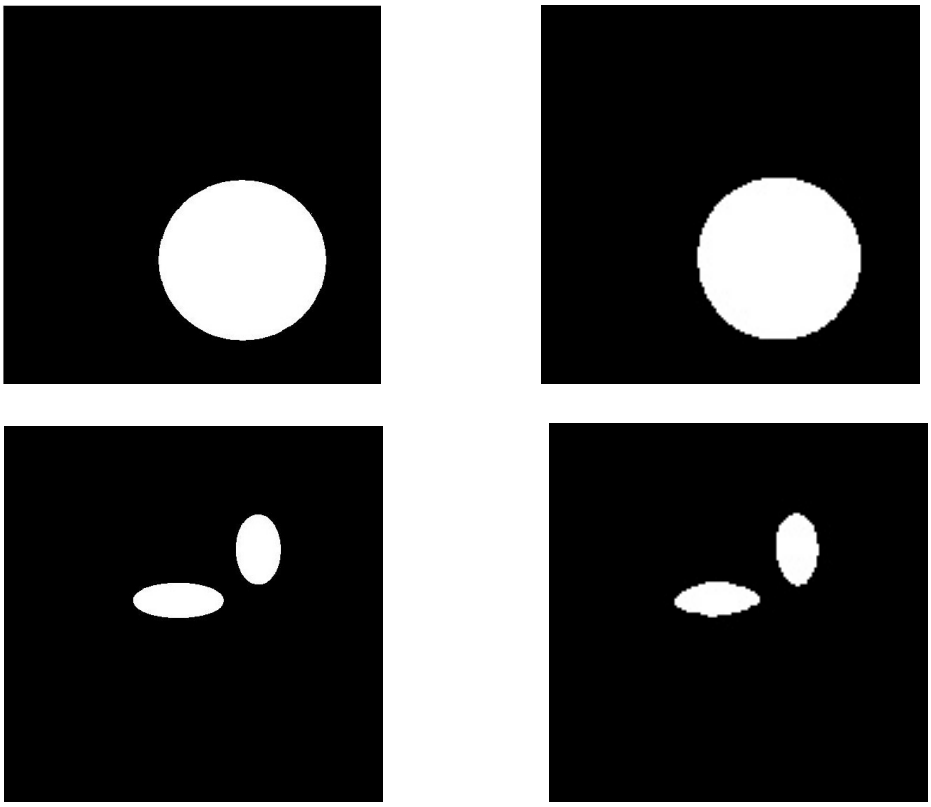

(a) True geometry (b) Combined method

Figure 3.4: Reconstruction of objects in the testing data set with $k = 6$ and $\theta = 90^o$: one disk (top) and two ellipses of similar sizes (bottom).

3.4.3 Reconstruction of objects outside the testing data set

In this part, we test the method for other types of objects with noisy scattering data. We added artificial noise to the scattering data obtained from solving the direct problem with wave number $k = 6$. Recall that the inverse problem with one incident wave is extremely ill-posed, and there was no artificial noise added to the scattering data in the training process. The tests with noisy data for non-elliptical objects show that the network can generalize its training to more realistic situations that are unseen from the training process. We first used

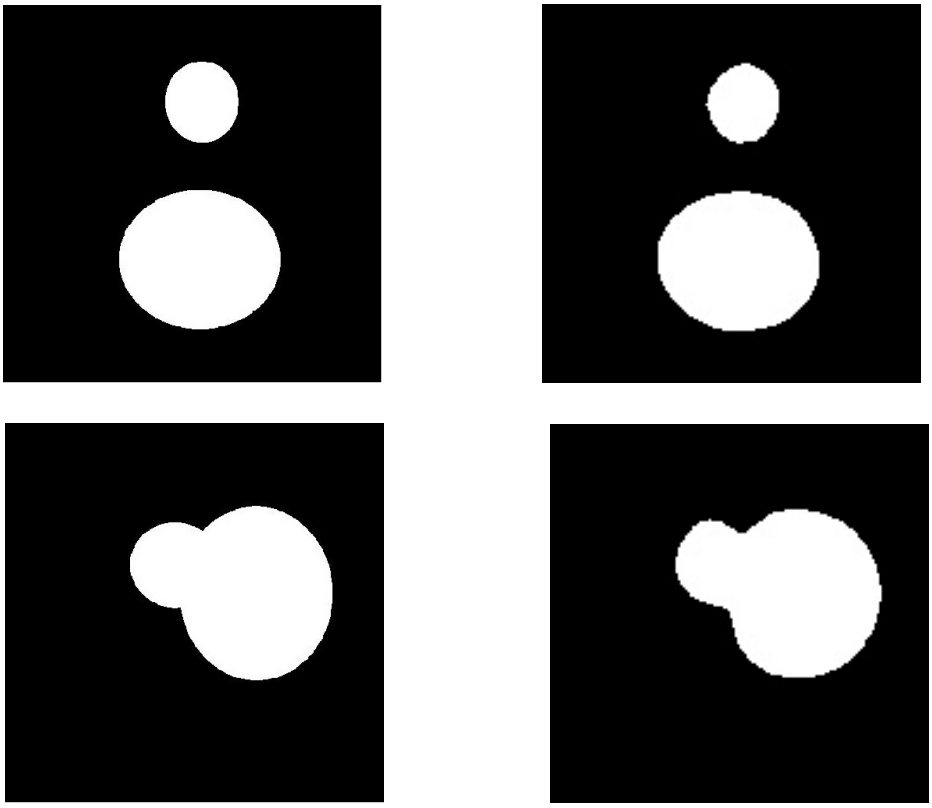

(a) True geometry (b) Combined method

Figure 3.5: Reconstruction of objects in the testing data set with $k = 6$ and $\theta = 45^o$: two ellipses of different sizes (top) and two overlapping ellipses (bottom).

the same incident direction as in training, $\theta = 90^o$, to reconstruct an L-shaped object, see Figure 3.6. The combined method was able to provide reasonable reconstructions for the L-shaped object with different levels of noise.

Next, in Figures 3.7-3.8, we test the method with different non-elliptical shapes and noisy scattering data associated with an incident direction different from what was used in the training process. This is to further assert its flexibility. Recall that we trained the neural network with $\theta = 90^o$ and $\theta = 45^o$. We reconstructed a T-shaped object, and an object consisting of a disk and a rectangle using incident direction $\theta = 220^o$. Again, we were able to get satisfactory results regardless of the circumstances.

For scattering data from a single incident direction and a fixed wave number, it is almost impossible not only for sampling methods but also for many other inversion methods to reconstruct the shape and location of extended objects. Therefore, these results show that the

deep neural network has significantly improved the reconstruction capability of the imaging function under lack of data. Moreover, they also show that the combined method is flexible, meaning it can work well in some situations that are unseen from the training process.

(a) True geometry (b) 5% noise (c) 15% noise

Figure 3.6: Reconstruction of an L-shaped object with $k = 6$ and $\theta = 90^o$, and different noise levels added to the scattering data: 5% and 15%.

(a) True geometry (b) 5% noise (c) 15% noise

Figure 3.7: Reconstruction of a T-shaped object with with $k = 6$ and $\theta = 220^o$, and different noise levels added to the scattering data: 5% and 15%.

(a) True geometry (b) 5% noise (c) 15% noise

Figure 3.8: Reconstruction of a rectangle and a disk with $k = 6$ and $\theta = 220^o$, and different noise levels added to the scattering data: 5% and 15%.

Chapter 4

Imaging 3D Objects for Maxwell's Equations with Experimental Data

4.1 Formulation of the electromagnetic inverse scattering problem

In this section, we consider the time-harmonic electromagnetic inverse scattering problem that aims to determine the shape and location of 3D objects from far-field measurements provided by the Fresnel Institute. Let $k > 0$ be a fixed wave number from a possibly anisotropic medium. Denote Ω as a bounded Lipschitz domain occupied by the medium. Let $\epsilon, \mu : \mathbb{R}^3 \to \mathbb{C}^{3\times 3}$ be the electric permittivity and the magnetic permeability of the medium, respectively. Assume that $\mathbb{R}^3\backslash\overline{\Omega}$ is connected, and ϵ, μ and μ^{-1} are functions in $[L^\infty(\mathbb{R}^3)]^{3\times 3}$. The domain outside of Ω is assumed to be homogeneous. We hence assume that $\epsilon = \mu = I_3$ in $\mathbb{R}^3\backslash\Omega$, where I_3 is the 3×3 identity matrix. Denote by $\mathbf{E}^{in}, \mathbf{E} : \mathbb{R}^3 \to \mathbb{C}^3$ the incident electric field and the total electric field, respectively. Let $\mathbf{u} := \mathbf{E} - \mathbf{E}^{in}$ be the

scattered electric field. We consider the following electromagnetic scattering problem

$$\operatorname{curl}\left[\mu^{-1}(\mathbf{x})\operatorname{curl}\mathbf{E}\right] - k^2\epsilon(\mathbf{x})\mathbf{E} = 0, \quad \text{in } \mathbb{R}^3, \tag{4.1.1}$$

$$\operatorname{curl}\mathbf{u} \times \frac{\mathbf{x}}{|\mathbf{x}|} - ik\mathbf{u} = \mathcal{O}(|\mathbf{x}|^{-2}), \quad \text{as } |\mathbf{x}| \to \infty, \tag{4.1.2}$$

where the Silver–Müller radiation condition (4.1.2) is assumed to hold uniformly with respect to $\mathbf{x}/|\mathbf{x}|$. We refer to[51] for the well-posedness of this scattering problem. To formulate the inverse scattering problem, we introduce some notations. Denoting $\widehat{\mathbf{x}} = \mathbf{x}/|\mathbf{x}|$, we define

$$\mathbb{S}^2 = \{\mathbf{x} \in \mathbb{R}^3 : |\mathbf{x}| = 1\}, \quad \mathbf{L}_t^2(\mathbb{S}^2) = \{\mathbf{v} \in [L^2(\mathbb{S}^2)]^3 : \widehat{\mathbf{x}} \cdot \mathbf{v}(\widehat{\mathbf{x}}) = 0, \quad \widehat{\mathbf{x}} \in \mathbb{S}^2\}.$$

We consider the incident plane wave

$$\mathbf{E}^{in}(\mathbf{x}, \mathbf{d}, \mathbf{q}) = \mathbf{q}e^{ik\mathbf{x}\cdot\mathbf{d}},$$

where $\mathbf{d} \in \mathbb{S}^2$ indicates the direction of the incident propagation and $\mathbf{q} \in \mathbb{R}^3$ is the polarization vector such that $\mathbf{q} \cdot \mathbf{d} = 0$. It is well-known that the corresponding scattered wave $\mathbf{u}(\mathbf{x}, \mathbf{d}, \mathbf{q})$ satisfies

$$\mathbf{u}(\mathbf{x}, \mathbf{d}, \mathbf{q}) = \frac{e^{ik|\mathbf{x}|}}{|\mathbf{x}|}\left(\mathbf{u}^\infty(\widehat{\mathbf{x}}, \mathbf{d}, \mathbf{q}) + \mathcal{O}(|\mathbf{x}|^{-2})\right), \text{ as } |\mathbf{x}| \to \infty, \tag{4.1.3}$$

uniformly in all directions $\widehat{\mathbf{x}} \in \mathbb{S}^2$. The function $\mathbf{u}^\infty(\widehat{\mathbf{x}}, \mathbf{d}, \mathbf{q})$, which belongs to $\mathbf{L}_t^2(\mathbb{S}^2)$ for each incident and observation direction, is called the far-field pattern. We are interested in the following inverse problem.

Inverse problem: Given measurements of $\mathbf{u}^\infty(\widehat{\mathbf{x}}, \mathbf{d}, \mathbf{q})$ for all $\widehat{\mathbf{x}}, \mathbf{d} \in \mathbb{S}^2$ at a fixed wave number k, determine the shape and location of the scatterer, in other words, the domain of Ω.

4.2 Modified OSM for non-magnetic anisotropic media

4.2.1 Factorization analysis

In this non-magnetic case, $\mu = I_3$. We rewrite (4.1.1) in terms of the scattered field $\mathbf{u}$ as

$$\operatorname{curl}\operatorname{curl}\mathbf{u} - k^2\epsilon(\mathbf{x})\mathbf{u} = k^2 P\mathbf{E}^{in}, \tag{4.2.1}$$

where the contrast P is defined by

$$P := \epsilon - I_3.$$

We now define the far-field operator $\mathcal{F} : \mathbf{L}_t^2(\mathbb{S}^2) \to \mathbf{L}_t^2(\mathbb{S}^2)$ and Herglotz operator $\mathcal{H} : \mathbf{L}_t^2(\mathbb{S}^2) \to [L^2(\Omega)]^3$ as

$$(\mathcal{F}\mathbf{g})(\widehat{\mathbf{x}}) = \int_{\mathbb{S}^2} \mathbf{u}^\infty(\widehat{\mathbf{x}}, \mathbf{d}, \mathbf{g}(\mathbf{d}))ds(\mathbf{d}), \quad (\mathcal{H}\mathbf{g})(\mathbf{x}) = \int_{\mathbb{S}^2} \mathbf{g}(\mathbf{d})e^{ik\mathbf{x}\cdot\mathbf{d}}ds(\mathbf{d}).$$

It is well-known that the Herglotz operator $\mathcal{H}$ is compact and injective. Its adjoint operator $\mathcal{H}^* : [L^2(\Omega)]^3 \to \mathbf{L}_t^2(\mathbb{S}^2)$ of $\mathcal{H}$ is given by

$$(\mathcal{H}^*\mathbf{f})(\mathbf{d}) = \mathbf{d} \times \int_\Omega \mathbf{f}(\mathbf{x})e^{-ik\mathbf{x}\cdot\mathbf{d}}d\mathbf{x} \times \mathbf{d}, \quad \mathbf{d} \in \mathbb{S}^2.$$

The solution operator $\mathcal{G} : [L^2(\Omega)]^3 \to \mathbf{L}_t^2(\mathbb{S}^2)$ is defined by

$$\mathcal{G}\mathbf{f} = \mathbf{v}^\infty, \tag{4.2.2}$$

where $\mathbf{v} \in H_{\text{loc}}(\operatorname{curl}, \mathbb{R}^3)$ is the solution to (4.1.2)-(4.2.1) with $\mathbf{E}^{in} = \mathbf{f}$. It is easy to see that $\mathcal{F}$ has the factorization

$$\mathcal{F} = \mathcal{G}\mathcal{H}. \tag{4.2.3}$$

We next define the operator $\mathcal{T} : [L^2(\Omega)]^3 \to [L^2(\Omega)]^3$ as

$$\mathcal{T}\mathbf{f} = k^2 P(\mathbf{f} + \mathbf{v}),$$

where again $\mathbf{v} \in H_{\text{loc}}(\text{curl}\,, \mathbb{R}^3)$ is the solution to (4.1.2)-(4.2.1) with $\mathbf{E}^{in} = \mathbf{f}$.

The operators defined above are all linear bounded operators, see[52]. It is also known from[52] that the solution operator $\mathcal{G}$ can be factorized as $\mathcal{G} = \mathcal{H}^*\mathcal{T}$. This leads to the following factorization for $\mathcal{F}$ as

$$\mathcal{F} = \mathcal{H}^*\mathcal{T}\mathcal{H}. \tag{4.2.4}$$

The following assumption on wave number k is necessary for the further results of the factorization analysis in[52], which is also needed for the modified OSM.

Assumption 1. We assume that the wave number k is not a transmission eigenvalue. That means the only solution to the homogeneous system in $[L^2(\Omega)]^3 \times [L^2(\Omega)]^3$

$$\begin{aligned} \text{curl}\,\text{curl}\,\mathbf{w} - k^2\epsilon\mathbf{w} &= 0 \text{ in } \Omega, \\ \text{curl}\,\text{curl}\,\mathbf{v} - k^2\mathbf{v} &= 0 \text{ in } \Omega, \\ \nu \times \mathbf{w} &= \nu \times \mathbf{v} \text{ on } \partial\Omega, \\ \nu \times \text{curl}\,\mathbf{w} &= \nu \times \text{curl}\,\mathbf{v} \text{ on } \partial\Omega, \end{aligned}$$

is the trivial solution.

It is well-known that the set of real transmission eigenvalues is at most discrete for a real-valued permittivity, see[53] for more details about the transmission eigenvalue problems. The following coercivity result from[54] is important for our theoretical analysis.

Lemma 4.2.1. *If either* $\text{Im}\,(P)$ *is uniformly positive definite or there is a constant* $\gamma > 0$ *such that* $\text{Re}\,(P) + \gamma\text{Im}\,(P)$ *is uniformly positive definite and* $\text{Im}\,(P)$ *is positive semidefinite, then* $\mathcal{T}$ *is coercive on Range*$(\mathcal{H})$.

We close this part with an important lemma for analyzing the imaging function defined in the next part.

Lemma 4.2.2. *There exists a positive constant $\sigma > 0$ such that*

$$|(\mathcal{F}\mathbf{g}, \mathbf{g})| \geq \sigma \|\mathcal{H}\mathbf{g}\|^2, \quad \text{for all } \mathbf{g} \in \mathbf{L}_t^2(\mathbb{S}^2).$$

Proof. Using the factorization of $\mathcal{F}$ in (4.2.4) and the coercive property of $\mathcal{T}$ we obtain

$$|(\mathcal{F}\mathbf{g}, \mathbf{g})| = |(\mathcal{H}^*\mathcal{T}\mathcal{H}\mathbf{g}, \mathbf{g})| = |(\mathcal{T}\mathcal{H}\mathbf{g}, \mathcal{H}\mathbf{g})| \geq \sigma \|\mathcal{H}\mathbf{g}\|^2.$$

This completes the proof. □

4.2.2 The imaging function and its properties

Let $\mathbf{z} \in \mathbb{R}^3$ be the sampling points in the imaging process and $\mathbf{p} \in \mathbb{R}^3$ be a fixed nonzero vector. We define the imaging function I_{MOSM} for the modified OSM as

$$I_{MOSM}(\mathbf{z}) := \int_{\mathbb{S}^2} \left| \int_{\mathbb{S}^2} \mathbf{u}^\infty(\widehat{\mathbf{x}}, \mathbf{d}, \mathbf{h}(\mathbf{d})) e^{-ik\mathbf{d}\cdot\mathbf{z}} ds(\mathbf{d}) \right|^2 ds(\widehat{\mathbf{x}}), \tag{4.2.5}$$

where

$$\mathbf{h}(\mathbf{d}) = \alpha_1 \mathbf{d} \times \mathbf{p} + \alpha_2 \mathbf{d} \times \mathbf{p} \times \mathbf{d},$$

with any $\alpha_1, \alpha_2 \in \mathbb{C}$ such that $|\alpha_1|^2 + |\alpha_2|^2 > 0$.

To analyze the behavior of the imaging function I_{MOSM}, it is necessary to connect I_{MOSM} with the far-field operator $\mathcal{F}$. This can be seen in the following lemma. An advantage of the modified function is that it allows us to connect to $\mathcal{F}$ directly and naturally, and thus enables the use of polarization vectors $\mathbf{h}(\mathbf{d})$ instead of only $(\mathbf{d} \times \mathbf{p}) \times \mathbf{d}$ as for the imaging function of the OSM in[27].

Lemma 4.2.3. *The imaging function I_{MOSM} satisfies*

$$I_{MOSM}(\mathbf{z}) = \|\mathcal{F}\phi_{\mathbf{z}}\|^2, \tag{4.2.6}$$

where $\phi_{\mathbf{z}}(\mathbf{d}) = \mathbf{h}(\mathbf{d})e^{-ik\mathbf{d}\cdot\mathbf{z}}$.

Proof. Recall that $\mathbf{h}(\mathbf{d}) = \alpha_1\mathbf{d}\times\mathbf{p}+\alpha_2\mathbf{d}\times\mathbf{p}\times\mathbf{d}$. It implies that $\phi_{\mathbf{z}}(\mathbf{d})\cdot\mathbf{d} = 0$ for all $\mathbf{d}\in\mathbb{S}^2$, hence $\phi_{\mathbf{z}} \in \mathbf{L}^2_t(\mathbb{S}^2)$. Now, since $\mathbf{u}^\infty(\widehat{\mathbf{x}}, \mathbf{d}, \mathbf{h}(\mathbf{d}))$ is linear in $\mathbf{h}$, we can rewrite the imaging function as

$$I_{MOSM}(\mathbf{z}) = \int_{\mathbb{S}^2} \left| \int_{\mathbb{S}^2} \mathbf{u}^\infty(\widehat{\mathbf{x}}, \mathbf{d}, \phi_{\mathbf{z}}(\mathbf{d}))ds(\mathbf{d}) \right|^2 ds(\widehat{\mathbf{x}}) = \|\mathcal{F}\phi_{\mathbf{z}}\|^2.$$

□

The following theorem is the main theorem for our analysis of the behavior of I_{MOSM}.

Theorem 4.2.4. *For all $\mathbf{z}\in\mathbb{R}^3$ the imaging function satisfies*

$$I_{MOSM} \le \|\mathcal{G}\|^2 \left(|\alpha_1|^2\|W_{\mathbf{z}}\|^2 + |\alpha_2|^2\|V_{\mathbf{z}}\|^2\right),$$

and

$$I_{MOSM} \ge \frac{\sigma^2}{\|\mathbf{h}\|^2}\left(|\alpha_1|^2\|W_{\mathbf{z}}\|^2 + |\alpha_2|^2\|V_{\mathbf{z}}\|^2\right)^2 > 0,$$

where $\mathbf{h}$ is given in (4.2.5), σ is the positive coercive constant in Lemma 4.2.2 and

$$W_{\mathbf{z}}(\mathbf{x}) = \widetilde{W}(\mathbf{z}-\mathbf{x}), \quad V_{\mathbf{z}}(\mathbf{x}) = \widetilde{V}(\mathbf{z}-\mathbf{x}), \quad \text{for all } \mathbf{x}\in\Omega, \tag{4.2.7}$$

with

$$\widetilde{W}(\mathbf{w}) = 4\pi i(\mathbf{w}\times\mathbf{p})\frac{\cos(k|\mathbf{w}|)-j_0(k|\mathbf{w}|)}{k|\mathbf{w}|^2}, \tag{4.2.8}$$

$$\begin{aligned}\widetilde{V}(\mathbf{w}) &= -4\pi\frac{\mathbf{p}|\mathbf{w}|^2-(\mathbf{p}\cdot\mathbf{w})\mathbf{w}}{|\mathbf{w}|^2}j_0(k|\mathbf{w}|)\\ &\quad + 12\pi\frac{(\mathbf{p}\cdot\mathbf{w})\mathbf{w}-\frac{1}{3}\mathbf{p}|\mathbf{w}|^2}{k^2|\mathbf{w}|^4}(\cos(k|\mathbf{w}|)-j_0(k|\mathbf{w}|)).\end{aligned} \tag{4.2.9}$$

Remark 4.2.5. The functions $|\widetilde{W}(\mathbf{z}-\mathbf{x})|^2, |\widetilde{V}(\mathbf{z}-\mathbf{x})|^2$ peak when $|\mathbf{z}-\mathbf{x}|<r$ for small $r>0$ and decay rapidly when $|\mathbf{z}-\mathbf{x}|>r$ (see Figure 4.1). This implies that $\|W_{\mathbf{z}}\|^2$ and $\|V_{\mathbf{z}}\|^2$ should have large values for $\mathbf{z}\in\Omega$ and are significantly small for $\mathbf{z}$ is away from Ω. See Figure 4.2 for an illustration of when Ω is a ball. We can also derive the decay rate as

$$I_{MOSM}(\mathbf{z}) = \mathcal{O}(\mathrm{dist}(\mathbf{z},\Omega)^{-2}) \quad \text{as } \mathrm{dist}(\mathbf{z},\Omega)\to\infty.$$

This Theorem shows that $I_{MOSM}(\mathbf{z})$ should work as an imaging function for the scatterer Ω and it works for all polarizations $\mathbf{h}(\mathbf{d}) = \alpha_1\mathbf{d}\times\mathbf{p}+\alpha_2\mathbf{d}\times\mathbf{p}\times\mathbf{d}$ with $|\alpha_1|^2+|\alpha_2|^2>0$. We now present its proof.

Proof. We recall a special form of the Funk–Hecke formula (see[55]) that is important for the proof

$$\int_{\mathbb{S}^2} e^{-ik\mathbf{d}\cdot\mathbf{z}}ds(\mathbf{d}) = 4\pi j_0(k|\mathbf{z}|), \tag{4.2.10}$$

where $j_0(t)=\sin(t)/t$ is the first kind of spherical Bessel function of order 0.
Using this integral formula we can calculate that

$$\begin{aligned}\int_{\mathbb{S}^2}\mathbf{d}\times\mathbf{p}e^{-ik\mathbf{d}\cdot\mathbf{z}}ds(\mathbf{d}) &= \frac{4\pi i}{k}\mathrm{curl}_{\mathbf{z}}(\mathbf{p}j_0(k|\mathbf{z}|)) = \widetilde{W}(\mathbf{z}),\\ \int_{\mathbb{S}^2}\mathbf{d}\times\mathbf{p}\times de^{-ik\mathbf{d}\cdot\mathbf{z}}ds(\mathbf{d}) &= -\frac{4\pi}{k^2}\mathrm{curl}^2_{\mathbf{z}}(\mathbf{p}j_0(k|\mathbf{z}|)) = \widetilde{V}(\mathbf{z}).\end{aligned}$$

It can be checked that $\widetilde{W}(\mathbf{z}) = \widetilde{V}(\mathbf{z}) = O(1/|\mathbf{z}|)$ as $|\mathbf{z}|\to\infty$. We define $W_{\mathbf{z}}(\mathbf{x}) := \widetilde{W}(\mathbf{z}-$

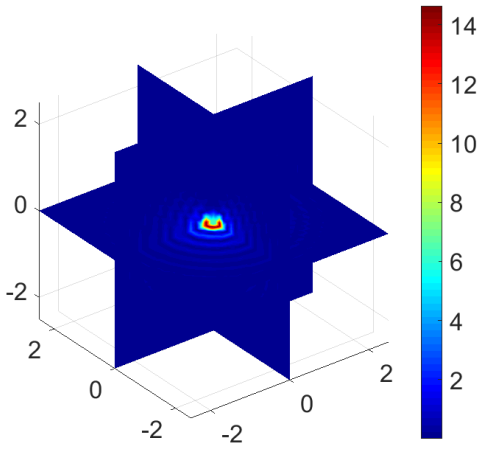

(a) $|\widetilde{W}|^2$

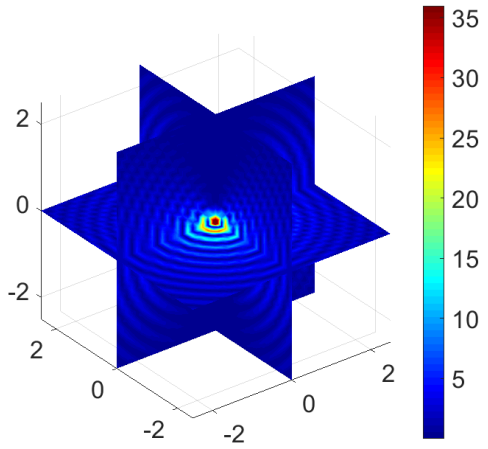

(b) $|\widetilde{V}|^2$

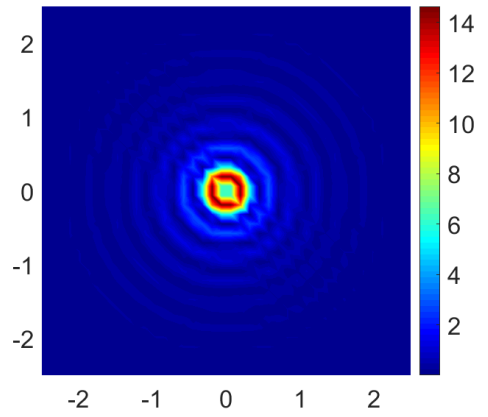

(c) Top view of (a)

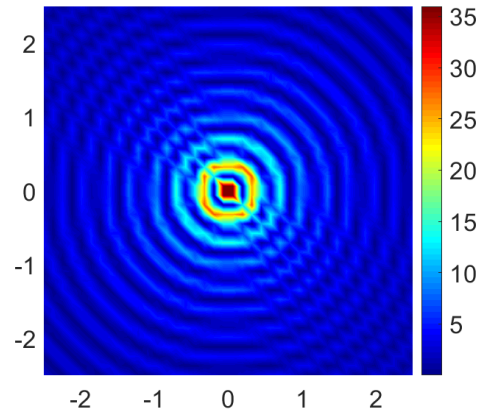

(d) Top view of (b)

Figure 4.1: An illustration of $|\widetilde{W}|^2, |\widetilde{V}|^2$ for $\mathbf{z} \in [-2.5, 2.5]^3, k = 10, \mathbf{p} = (0, 0, 1)$.

$\mathbf{x}), V_{\mathbf{z}}(\mathbf{x}) := \widetilde{V}(\mathbf{z} - \mathbf{x})$. Recall that $\phi_z(\mathbf{d}) = \mathbf{h}(\mathbf{d})e^{-ik\mathbf{d}\cdot\mathbf{z}}$. It follows from the definition of the Herglotz operator $\mathcal{H}$ that

$$\mathcal{H}\phi_{\mathbf{z}}(\mathbf{x}) = \alpha_1 W_{\mathbf{z}}(\mathbf{x}) + \alpha_2 V_{\mathbf{z}}(\mathbf{x}), \quad \mathbf{x} \in \Omega.$$

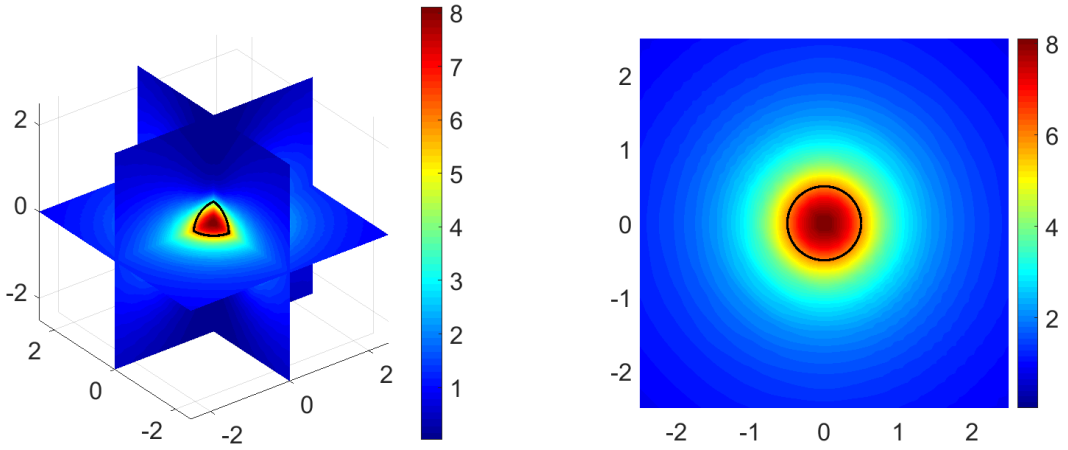

(a) $\|H\phi_z\|^2$ (b) Top view of (a)

Figure 4.2: An illustration of $\|H\phi_z\|^2$ for $\mathbf{z} \in [-2.5, 2.5]^3, \Omega = \{\mathbf{z} \in \mathbb{R}^3 : |\mathbf{z}| \leq 0.5\}, k = 10, \alpha_1 = \alpha_2 = 1, \mathbf{p} = (0, 0, 1)$.

Rewrite $\widetilde{V}(\mathbf{z})$ as

$$\widetilde{V}(\mathbf{z}) = \mathbf{z}\left(4\pi\frac{\mathbf{p}\cdot\mathbf{z}}{|\mathbf{z}|^2}j_0(k|\mathbf{z}|) + 12\pi\frac{\mathbf{p}\cdot\mathbf{z}}{k^2|\mathbf{z}|^4}(\cos(k|\mathbf{z}|) - j_0(k|\mathbf{z}|))\right) - \mathbf{p}\left(4\pi + 4\pi\frac{\cos(k|\mathbf{z}|) - j_0(k|\mathbf{z}|)}{k^2|\mathbf{z}|^2}\right),$$

thus we can deduce that

$$\overline{\widetilde{V}(\mathbf{z})} \cdot \widetilde{W}(\mathbf{z}) = 0, \quad \text{for all } \mathbf{z} \in \mathbb{R}^3.$$

Therefore,

$$\|\mathcal{H}\phi_{\mathbf{z}}\|^2 = |\alpha_1|^2\|W_{\mathbf{z}}\|^2 + |\alpha_2|^2\|V_{\mathbf{z}}\|^2. \tag{4.2.11}$$

Now consider $\mathbf{z} \in \mathbb{R}^3$, by Lemma 4.2.6 and the factorization of $\mathcal{F}$

$$I_{MOSM}(\mathbf{z}) \leq \|\mathcal{F}\phi_{\mathbf{z}}\|^2 \leq \|\mathcal{G}\|^2\|\mathcal{H}\phi_{\mathbf{z}}\|^2,$$

which implies the first estimate of the theorem.

From Lemma 4.2.3 and the Cauchy–Schwartz inequality, we have

$$\|\mathcal{F}\phi_{\mathbf{z}}\|\|\phi_{\mathbf{z}}\| \geq |(\mathcal{F}\phi_{\mathbf{z}}, \phi_{\mathbf{z}})| \geq \sigma\|\mathcal{H}\phi_{\mathbf{z}}\|^2.$$

Thus, using (4.2.11), the other estimate follows. This lower bound is strictly positive thanks to the injectivity of $\mathcal{H}$ and the relation (4.2.11). This completes the proof of the theorem. □

Now recall that the imaging function of the OSM studied in[27] is defined by

$$I_{OSM}(\mathbf{z}) = \int_{\mathbb{S}^2} \left| \int_{\mathbb{S}^2} \mathbf{u}^\infty(\widehat{\mathbf{x}}, \mathbf{d})((\mathbf{d} \times \mathbf{p}) \times \mathbf{d}) \cdot (\widehat{\mathbf{x}} \times \mathbf{p}) \times \widehat{\mathbf{x}} e^{ik\widehat{\mathbf{x}}\cdot\mathbf{z}} ds(\widehat{\mathbf{x}}) \right|^2 ds(\mathbf{d})$$

where $\mathbf{p} \in \mathbb{R}^3$ is some polarization vector. We provide a relation between the imaging functions I_{MOSM} and I_{OSM} in the case $\alpha_1 = 0$.

Corollary 4.2.6. *When $\alpha_1 = 0$, the two imaging functions satisfy*

$$I_{OSM}(\mathbf{z}) \leq \frac{|\mathbf{p}|^2}{|\alpha_2|^2} I_{MOSM}(\mathbf{z})$$

for all $\mathbf{z} \in \mathbb{R}^3$.

Proof. The proof follows from a combination of Lemmas 4 and 5 in[27], and the Cauchy–Schwarz inequality. □

This method is stable with respect to noise in the data. Indeed, assume that we only know the far-field data $\mathcal{F}$ up to a perturbation $\mathcal{F}_\delta$ such that

$$\|\mathcal{F} - \mathcal{F}_\delta\| \leq \delta\|\mathcal{F}\|,$$

for some $\delta > 0$. Denoting by $I_{MOSM,\delta}$, the imaging function corresponding to $\mathcal{F}_\delta$, we can derive the following stability estimate as in theorem 7 in[27]

Theorem 4.2.7. *The imaging functions I_{MOSM} and $I_{MOSM,\delta}$ satisfy*

$$|I_{MOSM}(\mathbf{z}) - I_{MOSM,\delta}(\mathbf{z})| \leq (\delta^2 + 2\delta)\|\mathcal{F}\|^2\|\mathbf{h}\|^2,$$

for all $\mathbf{z} \in \mathbb{R}^3$.

4.3 Modified OSM for magnetic anisotropic media

In this magnetic case, we have $\mu = \mu(x)$. As in the previous section, we first study the factorization analysis for the far-field operator and then analyze the imaging function for the modified OSM.

4.3.1 Factorization analysis

Recall that $P = \epsilon - I_3$. Denote $Q = I_3 - \mu^{-1}$. We rewrite the problem for the scattered field $\mathbf{u}$ as

$$\operatorname{curl}\operatorname{curl}\mathbf{u} - k^2\mathbf{u} = k^2P(\mathbf{f} + \mathbf{u}) + \operatorname{curl}[Q(\mathbf{g} + \operatorname{curl}\mathbf{u})], \quad \text{in } \mathbb{R}^3 \tag{4.3.1}$$

$$\operatorname{curl}\mathbf{u} \times \frac{\mathbf{x}}{|\mathbf{x}|} - ik\mathbf{u} = \mathcal{O}(|\mathbf{x}|^{-2}) \quad \text{as } |\mathbf{x}| \to \infty. \tag{4.3.2}$$

Here, the general $(\mathbf{f}, \mathbf{g}) \in [L^2(\Omega)]^3 \times [L^2(\Omega)]^3$ in the right-hand side is convenient for our presentation. If $(\mathbf{f}, \mathbf{g}) = (\mathbf{E}_{in}, \operatorname{curl}\mathbf{E}_{in})$, we have the original scattering problem. The following assumption is important for the analysis in this section.

Assumption 2. Assume that there exist $C_1, C_2 > 0$ such that for all $\mathbf{z} \in \mathbb{C}^3$

$$\operatorname{Im}(Q\mathbf{z} \cdot \overline{\mathbf{z}}) \geq C_1|\mathbf{z}|^2, \quad \operatorname{Im}(P\mathbf{z} \cdot \overline{\mathbf{z}}) \geq C_2|\mathbf{z}|^2,$$

almost everywhere in Ω.

Note that unlike in the non-magnetic case, this assumption excludes the transmission eigenvalues in the scattering problem. We now define the far-field operator $\mathcal{F} : \mathbf{L}_t^2(\mathbb{S}^2) \to$

$\mathbf{L}_t^2(\mathbb{S}^2)$ and the solution operator $G : [L^2(\Omega)]^3 \times [L^2(\Omega)]^3 \to \mathbf{L}_t^2(\mathbb{S}^2)$

$$(\mathcal{F}\mathbf{p})(\widehat{\mathbf{x}}) = \int_{\mathbb{S}^2} \mathbf{u}^\infty(\widehat{\mathbf{x}}, \mathbf{d}, \mathbf{p}(\mathbf{d}))ds(\mathbf{d}), \quad \mathcal{G}(\mathbf{f}, \mathbf{g}) = \mathbf{u}^\infty,$$

where $\mathbf{u}^\infty$ is the far-field pattern satisfying (4.1.3) and

$$\begin{aligned} &\int_{\mathbb{R}^2} \operatorname{curl} \mathbf{u} \cdot \operatorname{curl} \overline{\mathbf{v}} - k^2 \mathbf{u} \cdot \overline{\mathbf{v}} d\mathbf{x} \\ &= \int_\Omega [k^2 P(\mathbf{u} + \mathbf{f})] \cdot \overline{\mathbf{v}} d\mathbf{x} + \int_\Omega Q(\operatorname{curl} \mathbf{u} + \mathbf{g}) \cdot \operatorname{curl} \overline{\mathbf{v}} d\mathbf{x}, \end{aligned} \tag{4.3.3}$$

for all $\mathbf{v} \in H(\operatorname{curl}, \mathbb{R}^3)$ with compact support. It is known in[56] that equation (4.3.3) is equivalent to the integro-differential equation

$$\mathbf{u}(\mathbf{x}) = (k^2 + \nabla \operatorname{div}) \int_\Omega \Phi(\mathbf{x}, \mathbf{y})[P(\mathbf{u} + \mathbf{f})](\mathbf{y}) d\mathbf{y} + \operatorname{curl} \int_\Omega \Phi(\mathbf{x}, \mathbf{y})[Q(\operatorname{curl} \mathbf{u} + \mathbf{g})](\mathbf{y}) d\mathbf{y},$$

where $\Phi(\mathbf{x}, \mathbf{y}) = \exp(ik|\mathbf{x} - \mathbf{y}|)/(4\pi|\mathbf{x} - \mathbf{y}|)$ is the free-space Green function of the scalar Helmholtz equation. Let $\mathcal{H}_{1,2} : \mathbf{L}_t^2(\mathbb{S}^2) \to [L^2(\Omega)]^3$ be defined by

$$(\mathcal{H}_1 \mathbf{p})(\mathbf{y}) = \int_{\mathbb{S}^2} \mathbf{p}(\mathbf{d}) e^{ik\mathbf{d}\cdot\mathbf{y}} ds(\mathbf{d}) \quad \text{and} \quad \mathcal{H}_2 \mathbf{p} = \operatorname{curl} \mathcal{H}_1 \mathbf{p}.$$

The Herglotz operator $\mathcal{H} : \mathbf{L}_t^2(\mathbb{S}^2) \to [L_2(\Omega)]^3 \times [L^2(\Omega)]^3$ in the magnetic case is defined by

$$\mathcal{H}\mathbf{p} = (\mathcal{H}_1 \mathbf{p}, \mathcal{H}_2 \mathbf{p}). \tag{4.3.4}$$

The adjoint operators $\mathcal{H}_{1,2}^*$ of $\mathcal{H}_{1,2}$ are given by $\mathcal{H}_{1,2}^* : [L^2(\Omega)]^3 \to \mathbf{L}_t^2(\mathbb{S}^2)$

$$(\mathcal{H}_1^* \mathbf{g})(\mathbf{d}) = \mathbf{d} \times \int_\Omega \mathbf{g}(\mathbf{y}) e^{-ik\mathbf{d}\cdot\mathbf{y}} d\mathbf{y} \times \mathbf{d}, \quad (\mathcal{H}_2^* \mathbf{g})(\mathbf{d}) = ik\mathbf{d} \times \int_\Omega \mathbf{g}(\mathbf{y}) e^{-ik\mathbf{d}\cdot\mathbf{y}} d\mathbf{y}.$$

Then, the adjoint operator $\mathcal{H}^* : [L^2(\Omega)]^3 \times [L^2(\Omega)]^3 \to \mathbf{L}_t^2(\mathbb{S}^2)$ of the Herglotz operator is given by

$$\mathcal{H}^*(\mathbf{f}, \mathbf{g}) = \mathcal{H}_1^* \mathbf{f} + \mathcal{H}_2^* \mathbf{g}.$$

As in the non-magnetic case, we can factorize the far-field operator as

$$\mathcal{F} = \mathcal{G}\mathcal{H}.$$

For $(\mathbf{f}, \mathbf{g}) \in [L^2(\Omega)]^3 \times [L^2(\Omega)]^3$, the middle operator $\mathcal{T} : [L^2(\Omega)]^3 \times [L^2(\Omega)]^3 \to [L^2(\Omega)]^3 \times [L^2(\Omega)]^3$ is defined by

$$\mathcal{T}(\mathbf{f}, \mathbf{g}) := (k^2 P(\mathbf{u} + \mathbf{f}), Q(\operatorname{curl} \mathbf{u} + \mathbf{g})),$$

where $\mathbf{u}$ is the solution to (4.3.3) with $(\mathbf{f}, \mathbf{g})$ on the right-hand side.

Lemma 4.3.1. *The middle operator $\mathcal{T}$ is a linear bounded operator on $[L^2(\Omega)]^3 \times [L^2(\Omega)]^3$.*

Proof. Consider $(\tilde{\mathbf{f}}, \tilde{\mathbf{g}}) \in [L^2(\Omega)]^3 \times [L^2(\Omega)]^3$ and let $\tilde{\mathbf{u}}$ be the solution with this right-hand side in (4.3.3). Then,

$$\mathcal{T}(\tilde{\mathbf{f}}, \tilde{\mathbf{g}}) = (k^2 P(\tilde{\mathbf{u}} + \tilde{\mathbf{f}}), Q(\operatorname{curl} \tilde{\mathbf{u}} + \tilde{\mathbf{g}})),$$

Therefore, for any $a, b \in \mathbb{C}$, we obtain

$$\begin{aligned} a\mathcal{T}(\mathbf{f}, \mathbf{g}) + b\mathcal{T}(\tilde{\mathbf{f}}, \tilde{\mathbf{g}}) &= (k^2 P(b\tilde{\mathbf{u}} + a\mathbf{u} + b\tilde{\mathbf{f}} + a\mathbf{f}), Q(b\operatorname{curl} \tilde{\mathbf{u}} + a\operatorname{curl} \mathbf{u} + b\tilde{\mathbf{g}} + a\mathbf{g})) \\ &= T(a(\mathbf{f}, \mathbf{g}) + b(\tilde{\mathbf{f}}, \tilde{\mathbf{g}})), \end{aligned}$$

thanks to the linearity of the problem (4.3.3).

For $(\mathbf{f}, \mathbf{g}) \in [L^2(\Omega)]^3 \times [L^2(\Omega)]^3$, since (4.3.3) is well-posed, there exists a constant $C > 0$ such that

$$\|\mathbf{u}\|_{H(\operatorname{curl},\Omega)} \leq C\|(\mathbf{f}, \mathbf{g})\|.$$

We can deduce the boundedness of T from the following additional estimates

$$\begin{aligned} \|P(\mathbf{u} + \mathbf{f})\| &\leq \||P|_F\|_{L^\infty}(\|\mathbf{u}\|_{H(\operatorname{curl},\Omega)} + \|\mathbf{f}\|), \\ \|Q(\operatorname{curl} \mathbf{u} + \mathbf{g})\| &\leq \||Q|_F\|_{L^\infty}(\|\mathbf{u}\|_{H(\operatorname{curl},\Omega)} + \|\mathbf{g}\|), \end{aligned}$$

where $|\cdot|_F$ is the Frobenius matrix norm. This completes the proof. □

Lemma 4.3.2. *The far-field operator $\mathcal{F}$ can be factorized as*

$$\mathcal{F} = \mathcal{H}^*\mathcal{T}\mathcal{H}.$$

Proof. Since $\mathcal{F} = \mathcal{G}\mathcal{H}$, it is sufficient to show that $\mathcal{G} = \mathcal{H}^*\mathcal{T}$. We have

$$\begin{aligned}\mathcal{H}^*\mathcal{T}(\mathbf{f},\mathbf{g}) = \widehat{\mathbf{x}} \times \int_\Omega k^2[P(\mathbf{u}+\mathbf{f})](\mathbf{y})e^{-ik\widehat{\mathbf{x}}\cdot\mathbf{y}}d\mathbf{y} \times \widehat{\mathbf{x}} \\ + ik\widehat{\mathbf{x}} \times \int_\Omega [Q(\operatorname{curl}\mathbf{u}+\mathbf{g})](\mathbf{y})e^{-ik\widehat{\mathbf{x}}\cdot\mathbf{y}}d\mathbf{y}.\end{aligned}$$

It is known that[45] the right-hand side of the above equation is the far-field pattern of the scattered field $\mathbf{u}$ given by

$$\mathbf{u}(\mathbf{x}) = (k^2 + \nabla\operatorname{div}) \int_\Omega \Phi(\mathbf{x},\mathbf{y})[P(\mathbf{u}+\mathbf{f})](\mathbf{y})d\mathbf{y} + \operatorname{curl} \int_\Omega \Phi(\mathbf{x},\mathbf{y})[Q(\operatorname{curl}\mathbf{u}+\mathbf{g})](\mathbf{y})d\mathbf{y}.$$

This implies that $\mathcal{H}^*\mathcal{T}(\mathbf{f},\mathbf{g}) = \mathbf{u}^\infty = \mathcal{G}(\mathbf{f},\mathbf{g})$. Therefore, $\mathcal{G} = \mathcal{H}^*\mathcal{T}$. □

For the convenience of the presentation of the proof of the following theorem, we will use $(\cdot,\cdot)$ and $\|\cdot\|$ indistinctively for the inner product and norm of $[L^2(\Omega)]^3$ and $[L^2(\Omega)]^3\times[L^2(\Omega)]^3$.

Lemma 4.3.3. *There exists $\gamma > 0$ such that*

$$(\operatorname{Im}\mathcal{T}(\mathbf{f},\mathbf{g}),(\mathbf{f},\mathbf{g})) \geq \gamma\|(\mathbf{f},\mathbf{g})\|^2, \tag{4.3.5}$$

for all $(\mathbf{f},\mathbf{g}) \in$ Range$(\mathcal{H})$.

Proof. Denote $\mathbf{h}_1 = \mathbf{g} + \operatorname{curl}\mathbf{u}, \mathbf{h}_2 = \mathbf{f} + \mathbf{u}$. We have

$$\begin{aligned}(\mathcal{T}(\mathbf{f},\mathbf{g}),(\mathbf{f},\mathbf{g})) &= \int_\Omega Q\mathbf{h}_1 \cdot (\overline{\mathbf{h}}_1 - \operatorname{curl}\overline{\mathbf{u}})d\mathbf{x} + \int_\Omega k^2 P\mathbf{h}_2 \cdot (\overline{\mathbf{h}}_2 - \overline{\mathbf{u}})d\mathbf{x} \\ &= (Q\mathbf{h}_1,\mathbf{h}_1) + k^2(P\mathbf{h}_2,\mathbf{h}_2) - (Q\mathbf{h}_1,\operatorname{curl}\mathbf{u}) - k^2(P\mathbf{h}_2,\mathbf{u}).\end{aligned} \tag{4.3.6}$$

From Assumption 2 we obtain that

$$\mathrm{Im}\,(Q\mathbf{h}_1,\mathbf{h}_1)) + k^2\mathrm{Im}\,(P\mathbf{h}_2,\mathbf{h}_2) \geq C_1\|\mathbf{h}_1\|^2 + k^2C_2\|\mathbf{h}_2\|^2.$$

We now estimate the imaginary parts of the last two terms on the right-hand side of (4.3.6). Since u is the radiating solution to (4.3.3) we have

$$\int_{\mathbb{R}^3}(\mathrm{curl}\,\mathbf{u}\cdot\mathrm{curl}\,\overline{\mathbf{v}} - k^2\mathbf{u}\cdot\overline{\mathbf{v}})d\mathbf{x} = \int_\Omega (Q\mathbf{h}_1\cdot\mathrm{curl}\,\overline{\mathbf{v}} + k^2P\mathbf{h}_2\cdot\overline{\mathbf{v}})d\mathbf{x}. \tag{4.3.7}$$

for all $\mathbf{v}\in H(\mathrm{curl}\,,\mathbb{R}^3)$ with compact support.

Let ρ be a positive constant such that Ω is contained in the ball $\{\mathbf{x}\in\mathbb{R}^3 : |\mathbf{x}|<\rho\}$. Now we take $\mathbf{v}=\phi\mathbf{u}$ in (4.3.7) where $\phi\in\mathbb{C}^\infty(\mathbb{R}^3)$ is a cut-off function with $\phi=1$ for $|\mathbf{x}|<\rho$ and $\phi=0$ for $|\mathbf{x}|\geq 2\rho$, then

$$\begin{aligned}\int_\Omega Q\mathbf{h}_1\cdot\mathrm{curl}\,\overline{\mathbf{u}} + k^2P\mathbf{h}_2\cdot\overline{\mathbf{u}}d\mathbf{x} = &\int_{|\mathbf{x}|<\rho}|\mathrm{curl}\,\mathbf{u}|^2 - k^2|\mathbf{u}|^2d\mathbf{x}\\ &+\int_{\rho<|\mathbf{x}|<2\rho}\mathrm{curl}\,\mathbf{u}\cdot\mathrm{curl}\,(\phi\mathbf{u}) - k^2|\mathbf{u}|^2\phi d\mathbf{x}.\end{aligned}$$

Using Stokes' theorem and taking the imaginary part of the right-hand side of the above equation we obtain

$$\mathrm{Im}\int_\Omega Q\mathbf{h}_1\cdot\mathrm{curl}\,\overline{\mathbf{u}}d\mathbf{x} + k^2P\mathbf{h}_2\cdot\overline{\mathbf{u}}d\mathbf{x} = \mathrm{Im}\int_{|\mathbf{x}|=\rho}(\widehat{\mathbf{x}}\times\mathrm{curl}\,\mathbf{u})\cdot\overline{\mathbf{u}}ds(\mathbf{x}).$$

Using the radiation condition (4.1.2) and the asymptotic behavior (4.1.3), we obtain

$$\lim_{\rho\to\infty}\int_{|\mathbf{x}|=\rho}(\widehat{\mathbf{x}}\times\mathrm{curl}\,\mathbf{u})\cdot\overline{\mathbf{u}}ds(\mathbf{x}) = -\frac{ik}{(4\pi)^2}\int_{\mathbb{S}^2}|\mathbf{u}^\infty|^2ds(\mathbf{x}).$$

Therefore, we can now estimate the imaginary part of the left-hand side of (4.3.6) as

$$\mathrm{Im}\,(\mathcal{T}(\mathbf{f},\mathbf{g}),(\mathbf{f},\mathbf{g})) \geq C_1\|\mathbf{h}_1\|^2 + k^2C_2\|\mathbf{h}_2\|^2 + \frac{k}{(4\pi)^2}\int_{\mathbb{S}^2}|\mathbf{u}^\infty|^2ds(\mathbf{x}).$$

From the fact that $(\operatorname{Im}\mathcal{T}(\mathbf{f},\mathbf{g}),(\mathbf{f},\mathbf{g})) = \operatorname{Im}(\mathcal{T}(\mathbf{f},\mathbf{g}),(\mathbf{f},\mathbf{g}))$, we imply

$$\operatorname{Im}(\mathcal{T}(\mathbf{f},\mathbf{g}),(\mathbf{f},\mathbf{g})) \geq C_1\|\mathbf{h}_1\|^2 + k^2 C_2\|\mathbf{h}_2\|^2.$$

Now assume that there is no $\gamma > 0$ such that (4.3.5) holds. Then, there exists a sequence $\{(\mathbf{f}_j,\mathbf{g}_j)\}_j \subset [L^2(\Omega)]^3 \times [L^2(\Omega)]^3$ such that $(\mathbf{f}_j,\mathbf{g}_j) = 1$ and

$$(\operatorname{Im}\mathcal{T}(\mathbf{f}_j,\mathbf{g}_j),(\mathbf{f}_j,\mathbf{g}_j)) \to 0 \text{ as } j \to \infty.$$

Then, it follows $\mathbf{h}_1^{\{j\}} = \mathbf{f}_j + \operatorname{curl}\mathbf{u}_j \to 0$ and $\mathbf{h}_2^{\{j\}} = \mathbf{g}_j + \mathbf{u}_j \to 0$ in $[L^2(\Omega)]^3$ as $j \to \infty$, where $\mathbf{u}_j$ is the solution to

$$\mathbf{u}_j(\mathbf{x}) = (k^2 + \nabla\operatorname{div})\int_\Omega [P(\mathbf{u}_j + \mathbf{f}_j)]\Phi(\mathbf{x},\mathbf{y})d\mathbf{y} + \operatorname{curl}\int_\Omega [Q(\operatorname{curl}\mathbf{u}_j + \mathbf{g}_j)]\Phi(\mathbf{x},\mathbf{y})d\mathbf{y}.$$

By the boundedness of the integro-differential operators (see[56]), we obtain

$$\|\mathbf{u}_j\|_{H(\operatorname{curl},\Omega)} \leq C_3(\||P|_F\|_{L^\infty}\|\mathbf{g}_j + \mathbf{u}_j\|) + C_4(\||Q|_F\|_{L^\infty}\|\mathbf{f}_j + \operatorname{curl}\mathbf{u}_j\|),$$

where C_3 and C_4 are positive constants. Thus $\mathbf{u}_j \to 0$ as $j \to \infty$ in $H(\operatorname{curl},\Omega)$ and therefore $(\mathbf{f}_j,\mathbf{g}_j) \to 0$ as $j \to \infty$ in $[L^2(\Omega)]^3 \times [L^2(\Omega)]^3$. The latter is a contradiction with $\|(\mathbf{f}_j,\mathbf{g}_j)\| = 1$. □

From this coercivity property and the factorization of $\mathcal{F}$, the following lemma, which is similar to Lemma 4.2.2, is satisfied in the magnetic case.

Lemma 4.3.4. *There exists a positive constant $\gamma > 0$ such that*

$$|(\mathcal{F}\mathbf{g},\mathbf{g})| \geq \gamma\|\mathcal{H}\mathbf{g}\|^2,$$

for all $\mathbf{g} \in \mathbf{L}_t^2(\mathbb{S}^2)$.

This lemma is again important for the analysis of the imaging function in the next part.

4.3.2 The imaging function and its properties

We consider the same imaging function $I_{MOSM}(\mathbf{z})$ and this function also satisfies Lemma 4.2.6. We now prove the main theorem for the analysis of the imaging function in the magnetic case.

Theorem 4.3.5. *For all $\mathbf{z} \in \mathbb{R}^3$ the imaging function satisfies*

$$I_{MOSM}(\mathbf{z}) \leq \|\mathcal{G}\|^2[(|\alpha_1|^2 + k^2|\alpha_2|^2)\|W_{\mathbf{z}}\|^2 + (k^2|\alpha_1|^2 + |\alpha_2|^2)\|V_{\mathbf{z}}\|^2],$$

and

$$I_{MOSM}(\mathbf{z}) \geq \frac{\gamma^2}{\|\mathbf{h}\|^2}[(|\alpha_1|^2 + k^2|\alpha_2|^2)\|W_{\mathbf{z}}\|^2 + (k^2|\alpha_1|^2 + |\alpha_2|^2)\|V_{\mathbf{z}}\|^2]^2 > 0,$$

where $\mathbf{h}$ is given in (4.2.5), γ is the positive constant in Lemma 4.3.4, and $W_{\mathbf{z}}, V_{\mathbf{z}}$ are given by (4.2.7).

Proof. Due to the presence of $\mathcal{H}_2$ in the Herglotz operator $\mathcal{H}$ in (4.3.4) we need to calculate curl $\int_{\mathbb{S}^2} \mathbf{d} \times \mathbf{p} e^{-ik\mathbf{d}\cdot\mathbf{z}} ds(\mathbf{d})$ and curl $\int_{\mathbb{S}^2} (\mathbf{d} \times \mathbf{p}) \times \mathbf{d} e^{-ik\mathbf{d}\cdot\mathbf{z}} ds(\mathbf{d})$. Using the formula (4.2.10) again, we derive

$$\text{curl} \int_{\mathbb{S}^2} \mathbf{d} \times \mathbf{p} e^{-ik\mathbf{d}\cdot\mathbf{z}} ds(\mathbf{d}) = \frac{4\pi i}{k} \text{curl}\,_{\mathbf{z}}^2(\mathbf{p} j_0(k|\mathbf{z}|)) = -ik\widetilde{V}(\mathbf{z}),$$

where $\widetilde{V}(\mathbf{z})$ is given by (4.2.9). Using (4.2.10) and the facts curl $^2 = -\Delta + \nabla\text{div}$, $\Delta j_0(k|\mathbf{z}|) + k^2 j_0(k|\mathbf{z}|) = 0$, we can compute

$$\begin{aligned}
\text{curl} \int_{\mathbb{S}^2} (\mathbf{d} \times \mathbf{p}) \times \mathbf{d} e^{-ik\mathbf{d}\cdot\mathbf{z}} ds(\mathbf{d}) &= \frac{-4\pi}{k^2} \text{curl}\,_{\mathbf{z}}^3(\mathbf{p} j_0(k|\mathbf{z}|)) \\
&= \frac{4\pi}{k^2} \text{curl}\,_z(\mathbf{p}\Delta j_0(k|\mathbf{z}|)) \\
&= -4\pi \text{curl}\,_z(\mathbf{p} j_0(k|\mathbf{z}|)) = ik\widetilde{W}(\mathbf{z}),
\end{aligned}$$

where $\widetilde{W}(\mathbf{z})$ is given by (4.2.8).

Recall $W_{\mathbf{z}}, V_{\mathbf{z}}$ from (4.2.7) and $\mathcal{H}_1\phi_{\mathbf{z}} = \alpha_1 W_{\mathbf{z}} + \alpha_2 V_{\mathbf{z}}$. Thanks to the above calculations,

we derive that

$$\mathcal{H}\phi_{\mathbf{z}} = (\alpha_1 W_{\mathbf{z}} + \alpha_2 V_{\mathbf{z}}, \alpha_1 ikV_{\mathbf{z}} - \alpha_2 ikW_{\mathbf{z}}).$$

As proven in the proof of Theorem 4.2.4, $W_{\mathbf{z}}$ and $V_{\mathbf{z}}$ are orthogonal. Therefore, we have

$$\begin{aligned}\|\mathcal{H}\phi_{\mathbf{z}}\|^2 &= \|\alpha_1 W_{\mathbf{z}} + \alpha_2 V_{\mathbf{z}}\|^2 + \|\alpha_1 ikV_{\mathbf{z}} - \alpha_2 ikW_{\mathbf{z}}\|^2 \\ &= (|\alpha_1|^2 + k^2|\alpha_2|^2)\|W_{\mathbf{z}}\|^2 + (k^2|\alpha_1|^2 + |\alpha_2|^2)\|V_{\mathbf{z}}\|^2.\end{aligned}$$

Recall from Lemma 4.2.6 that $I_{MOSM}(\mathbf{z}) = \|\mathcal{F}\phi_{\mathbf{z}}\|^2$. As in the proof of Theorem 4.2.4, we complete the proof of this theorem using the following inequalities

$$\frac{\sigma^2}{\|\mathbf{h}\|^2}\|\mathcal{H}\phi_{\mathbf{z}}\|^4 \leq \|\mathcal{F}\phi_{\mathbf{z}}\|^2 \leq \|\mathcal{G}\|^2\|\mathcal{H}\phi_{\mathbf{z}}\|^2.$$

Here, the first inequality follows from the Cauchy–Schwarz inequality and Lemma 4.3.4, and the second inequality follows from the factorization of $\mathcal{F}$. □

We also have similar properties of the imaging function as in Corollary 4.2.6 and Theorem 4.2.7.

4.4 Numerical results

We apply the classical FM[57], the OSM in[27] and the modified OSM to invert the 3D experimental database provided by the Fresnel Institute, France[58]. More precisely, we invert the calibrated co-polarized datasets (TwoSpheres-PP, TwoCubes-PP, Cylinder-PP, CubeSpheres-PP, IsocaSphere-PP) for all the examples in this section. The sampling methods are implemented using the computing software Matlab. We rescale 40 mm to be 1 unit of length in our Matlab simulations. From now on we will use scaled lengths in the presentation instead of actual lengths, for example, 2 instead of 80 mm. The sampling domain is the cube $[-2.5, 2.5]^3$ uniformly divided into $32 \times 32 \times 32$ sampling points. The far-field pattern is computed from the measured scattered field via (4.1.3). The distance from the

origin to the receivers (and the sources) is 44.9, which is large enough to guarantee a good approximation in (4.1.3).

In the experiments the targets are illuminated by 81 incident sources that are located far away, see Figure 4.3(a) for the distribution of the sources. However, due to technical reasons, the scattered electric field was collected at only 36 points on $\mathbb{S}^2 \cap \{\mathbf{z} = 0\}$, see Figure 4.3(b), and only the third component of the scattered field was measured. This is certainly the main challenge for the sampling methods which typically require full-aperture data. When computing the integrals to evaluate the imaging functions, the points where no data is present are treated as 0. Note that the measured data can be enhanced using the reciprocity property of the far-field pattern, but here we would like to test the performance of the sampling methods for the original limited-aperture data.

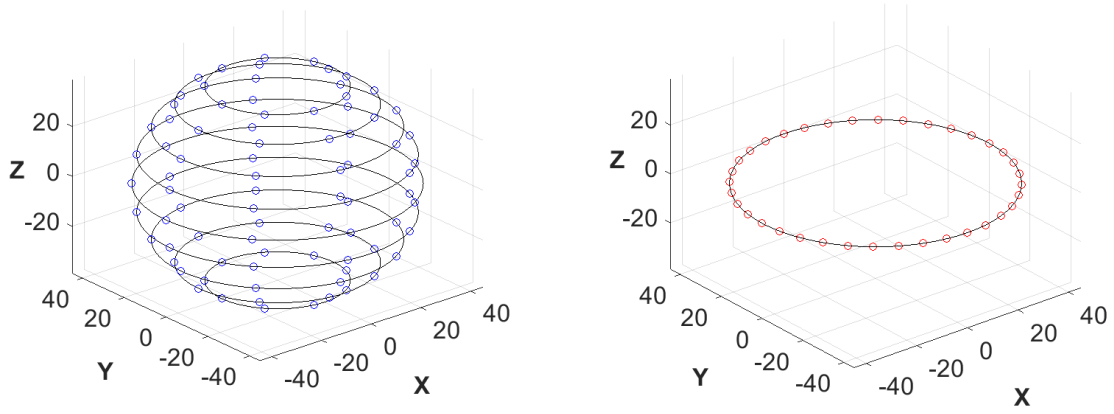

(a) Sources (b) Receivers

Figure 4.3: The experimental setup for incident sources and data receivers.

To help the readers understand better the reconstruction results, we use the information provided by the Fresnel Institute to create 3D objects mimicking the true 3D targets used in the experiments. The isovalue used in the 3D isosurface plotting for the case of IsocaSphere is 0.78 (78% of the maximal value of the imaging functions that are normalized). This isovalue is 0.5 in all of the other cases.

The real data should correspond to the non-magnetic case ($\mu = I_3$). The analysis of

the MOSM in this case requires Assumption 1 about the transmission eigenvalues. Finding these eigenvalues is by far a nontrivial task, see[59]. Thus we cannot verify whether the wave numbers used in the real data validation are transmission eigenvalues. However, the chance of having these transmission eigenvalues could be small since it is known that the set of such eigenvalues is at most a discrete set. Furthermore, Assumption 2 may not hold for the real data since the imaginary part of the permittivity ϵ is probably small and negligible according to[58].

TwoSpheres-PP dataset (Figure 4.4) and Cylinder-PP dataset (Figure 4.5). For the first two datasets, we can see that the OSM seems to be able to reconstruct only information in the (x, y)-plane of the targets. This can be due to the lack of measured data in the z-direction. However, the FM and the MOSM are able to provide more reasonable reconstructions. The FM can locate the targets but fails to provide reasonable shapes, while the MOSM can not only locate targets but also provide a good shape reconstruction in the case of the TwoSpheres-PP dataset. Its result for the Cylinder-PP dataset also looks more reasonable than that of the FM. The cylinder object has the largest volume among all the targets and is challenging to reconstruct. Only the data set at 3 GHz gives a reasonable result for this target.

TwoCubes-PP dataset (Figure 4.6), CubeSpheres-PP dataset (Figure 4.7). For these datasets the OSM provides similar performance as in the first two cases. It fails to reconstruct the z-direction of the targets. The reconstruction results of the FM again can provide the location of the targets. Moreover, the FM can even resolve and provide a reasonable size of the two cubes for the TwoCubes-PP dataset, see Figure 4.3(b). From the reconstruction results of the MOSM, we can see that the MOSM are again slightly better than those of the FM. The MOSM can locate the targets and provide more accurate information about the shape of the targets.

IsocaSphere-PP dataset (Figure 4.8). This is also known as the Mystery object and is the most complex in the database. It consists of twelve small spheres but is not as evenly distributed as those of the CubeSpheres-PP dataset. Compared with the OSM and FM, the MOSM again performs better. The OSM again fails to image the z-direction of the target

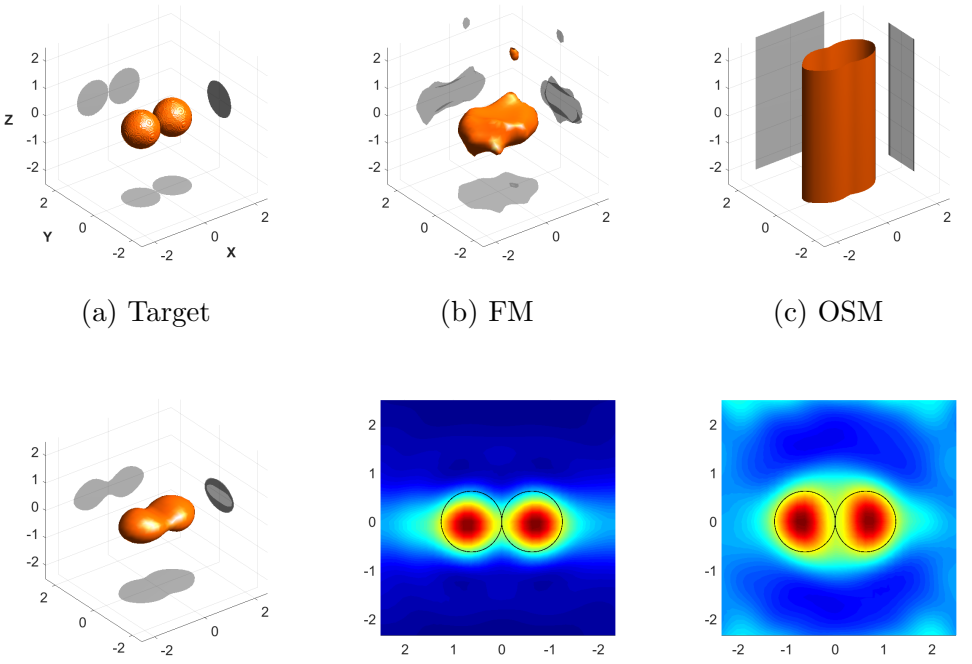

(a) Target (b) FM (c) OSM

(d) MOSM (e) MOSM on $\{y = 0\}$ (f) MOSM on $\{z = 0\}$

Figure 4.4: Reconstruction with TwoSpheres-PP dataset at 4 GHz.

while the FM cannot reconstruct any information for this case. The MOSM can recover the location of the target and provide a rough estimate of the shape of the target in the (x, y)-plane.

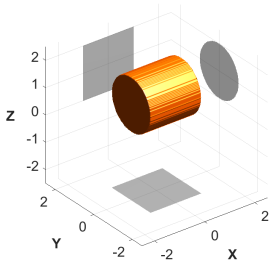

(a) Target

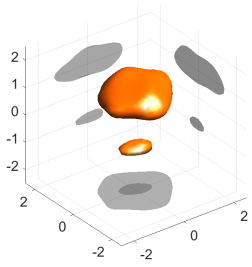

(b) FM

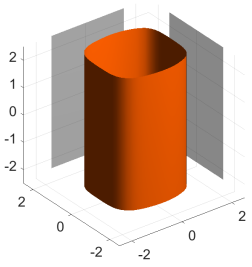

(c) OSM

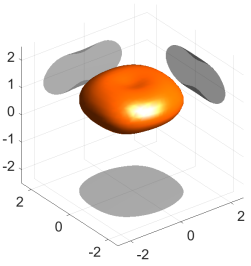

(d) MOSM

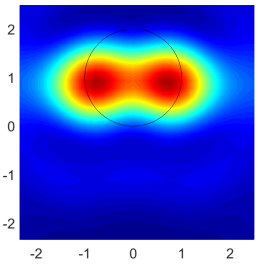

(e) MOSM on $\{x = 0\}$

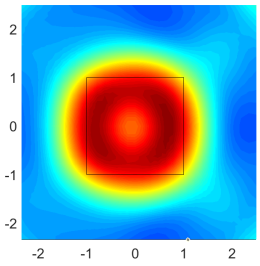

(f) MOSM on $\{z = 0\}$

Figure 4.5: Reconstruction with Cylinder-PP dataset at 3 GHz.

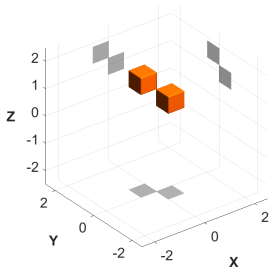

(a) Target

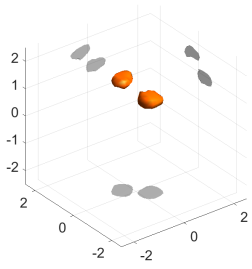

(b) FM

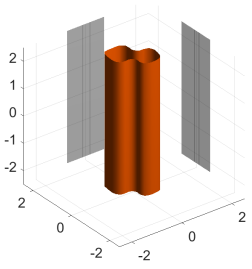

(c) OSM

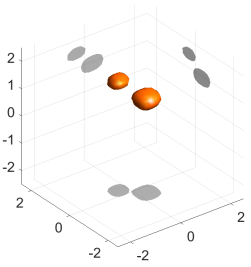

(d) MOSM

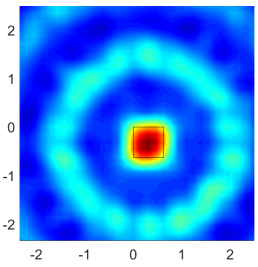

(e) MOSM on $\{z = 0.9\}$

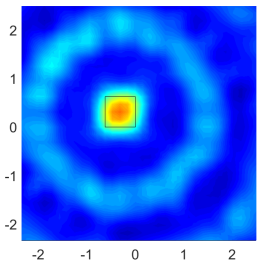

(f) MOSM on $\{z = 1.6\}$

Figure 4.6: Reconstruction with TwoCubes-PP dataset at 7.5 GHz.

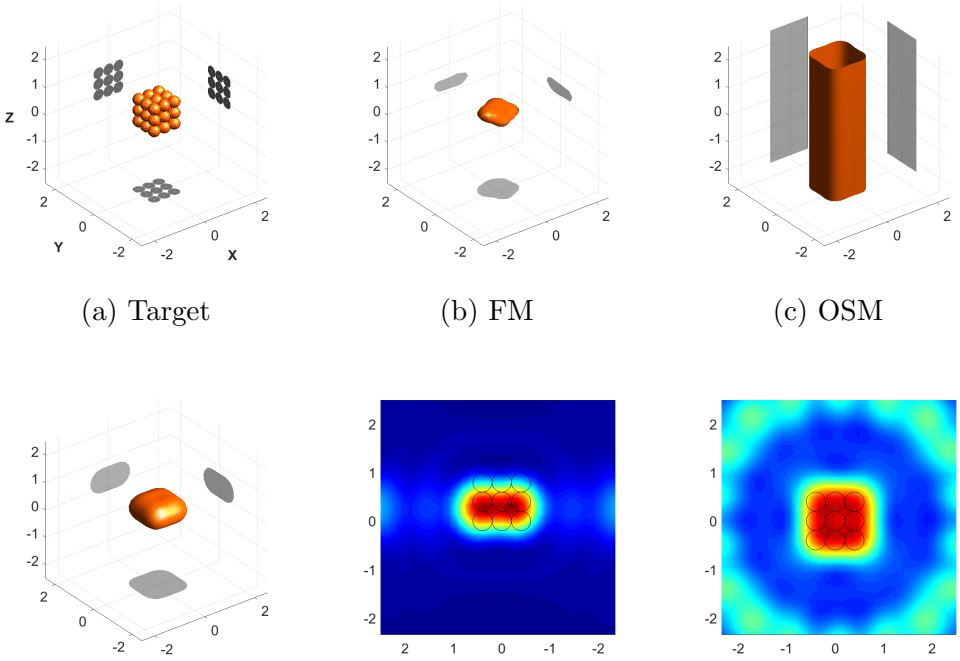

(a) Target (b) FM (c) OSM

(d) MOSM (e) MOSM on $\{y = 0\}$ (f) MOSM on $\{z = 0.4\}$

Figure 4.7: Reconstruction with CubeSpheres-PP dataset at 4.75 GHz.

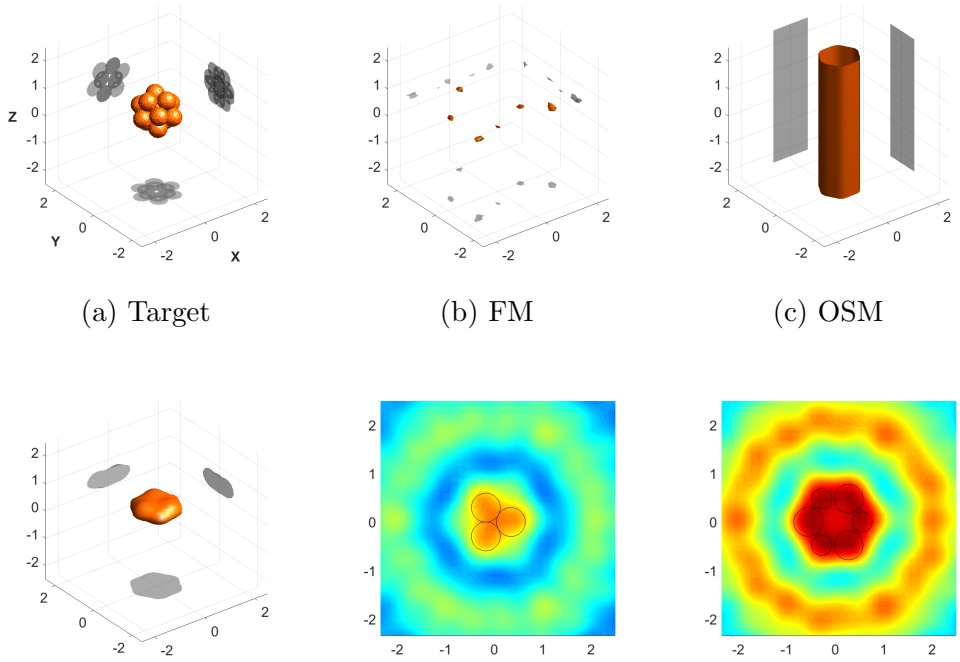

(a) Target (b) FM (c) OSM

(d) MOSM (e) MOSM on $\{z = 0\}$ (f) MOSM on $\{z = 0.4\}$

Figure 4.8: Reconstruction with IsocaSphere-PP dataset at 5.75 GHz.

Chapter 5

Conclusion

In conclusion, this work presents fast and stable numerical methods for solving inverse source and scattering problems associated with time-harmonic acoustic and electromagnetic waves.

In chapter 2, we introduce a sampling-type method for solving the acoustic inverse source problem for the Helmholtz equation at a fixed frequency from Cauchy data. We justify the behavior of the new imaging function, provide stability estimation, and present numerical results in 2D. The method accurately locates point sources and determines their intensities with a low relative error of $1 - 10\%$. We also extend the results to locate small volume sources using the asymptotic expansion of the radiated field. Compared to existing inversion techniques, this method is more computationally efficient and robust against noise.

In chapter 3, we successfully combine a sampling-type technique with a U-net Xception deep neural network to address the challenges of solving the inverse scattering problem using one incident wave data at a fixed frequency. We expand the analysis of the imaging function from chapter 2 and relate it to the original OSM. The combined method accurately inverts objects similar to those in the training dataset and complex objects with differing geometries from the training set. It is applicable to both near-field and far-field measurements. Additionally, the results remain efficient and robust despite variations in the incident wave or noise in the testing data.

In chapter 4, we analyze a modified version of the OSM studied in[27] for both non-magnetic

and magnetic cases for anisotropic Maxwell's equations. Compared with its original version the modified OSM is proved to be applicable to more types of polarizations associated with the electromagnetic scattering data. We provide a validation of the modified OSM, its original version, and the FM for 3D experimental data from the Fresnel database. The results indicate that the modified OSM performs better than the other two methods and is a promising imaging approach in inverse scattering.

Moving forward, we plan to extend these theoretical and numerical results to solve more general and complex inverse problems. For inverse source problems, we will address the challenging task of identifying sources with significantly different magnitudes of intensity. We will also study more complex problem settings, including inverse source problems for electromagnetic and elastic waves, as well as those in waveguide domains. For inverse scattering problems, we plan to extend and enhance sampling-type techniques to reconstruct more complex scatterers, such as electromagnetic bi-anisotropic media with general constitutive relations. We are also interested in studying inverse scattering problems associated with elastic waves in both two and three dimensions. Furthermore, we intend to combine these inversion methods with machine learning to address questions that traditional methods cannot tackle.

Bibliography

[1] T. Le, D.-L. Nguyen, H. Schmidt, and T. Truong. Imaging of 3D objects with experimental data using orthogonality sampling methods. *Inverse Problems*, 38:025007, 2022.

[2] T. Le, D.-L. Nguyen, V. Nguyen, and T. Truong. Sampling type method combined with deep learning for inverse scattering with one incident wave. *AMS Contemp. Math.*, 784: 63–80, 2023.

[3] I. Harris, T. Le, and D.-L. Nguyen. On reconstruction of small sources from cauchy data at a fixed frequency. *Appl. Math. Lett.*, 145:108765, 2023.

[4] A. Zaoui, H. Menana, M. Feliachi, and G. Berthiau. Inverse problem in nondestructive testing using arrayed eddy current sensors. *Sensors*, 10:8696–8704, 2010.

[5] S. Asadzadeh, T. Y. Rezaii, S. Beheshti, A. Delpak, and S. Meshgini. A systematic review of eeg source localization techniques and their applications on diagnosis of brain abnormalities. *J. Neurosci. Methods*, 339:108740, 2020.

[6] G. Bao, H. Ammari, and J. L. Fleming. An inverse source problem for Maxwell's equations in magnetoencephalography. *SIAM J. Appl. Math.*, 62:1369–1382, 2002.

[7] J. Tromp. Seismic wavefield imaging of Earth's interior across scales. *Nat. Rev. Earth Environ.*, 1:40–53, 2019.

[8] C. A. Balanis. *Antenna theory: analysis and design*. John wiley & sons, 2016.

[9] D. Liu, R. J. Garbacz, and D. M. Pozar. Antenna synthesis and optimization using generalized characteristic modes. *IEEE Trans. Antennas Propag.*, 38:862–868, 1990.

[10] A. E. Badia and T. Ha-Duong. On an inverse source problem for the heat equation. application to a pollution detection problem. *J. Inverse Ill-Posed Probl.*, 10:585–599, 2002.

[11] A. V. Kuzhuget, L. Beilina, M. V. Klibanov, A. Sullivan, L. Nguyen, and M. A. Fiddy. Blind backscattering experimental data collected in the field and an approximately globally convergent inverse algorithm. *Inverse Problems*, 28:095007, 2012.

[12] C. Alves and T. Ha-Duong. On inverse scattering by screens. *Inverse Problems*, 13: 1161–1176, 1997.

[13] F. Cakoni, D. Colton, and E. Darrigrand. The inverse electromagnetic scattering problem for screens. *Inverse Problems*, 19:627, 2003.

[14] R. Potthast. A study on orthogonality sampling. *Inverse Problems*, 26:074015, 2010.

[15] C. Y. Ahn, S. Chae, and W.-K. Park. Fast identification of short, sound-soft open arcs by the orthogonality sampling method in the limited-aperture inverse scattering problem. *Appl. Math. Lett.*, 109:106556, 2020.

[16] M. Akinci, M. Cayoren, and I. Akduman. Near-field orthogonality sampling method for microwave imaging: Theory and experimental verification. *IEEE Trans. Microw. Theory Tech.*, 64:2489, 2016.

[17] R. Griesmaier. Multi-frequency orthogonality sampling for inverse obstacle scattering problems. *Inverse Problems*, 27:085005, 2011.

[18] I. Harris and A. Kleefeld. Analysis of new direct sampling indicators for far-field measurements. *Inverse Problems*, 35:054002, 2019.

[19] X. Liu. A novel sampling method for multiple multiscale targets from scattering amplitudes at a fixed frequency. *Inverse Problems*, 33:085011, 2017.

[20] K. Ito, B. Jin, and J. Zou. A direct sampling method to an inverse medium scattering problem. *Inverse Problems*, 28:025003, 2012.

[21] J. Li and J. Zou. A direct sampling method for inverse scattering using far-field data. *Inverse Probl. Imaging*, 7:757–775, 2013.

[22] D. Zhang, Y. Guo, J. Li, and H. Liu. Locating multiple multipolar acoustic sources using the direct sampling method. *Commun. Comput. Phys.*, 25:1328–1356, 2019.

[23] R. Potthast. A fast new method to solve inverse scattering problems. *Inverse Problems*, 12:731–742, 1996.

[24] D. Colton and H. Haddar. An application of the reciprocity gap functional to inverse scattering theory. *Inverse Problems*, 21:383–398, 2005.

[25] L. Audibert and H. Haddar. A generalized formulation of the linear sampling method with exact characterization of targets in terms of farfield measurements. *Inverse Problems*, 30:035011, 2014.

[26] R. Potthast. Electromagnetic scattering from an orthotropic medium. *J. Int. Eq and Appl.*, 11:179–215, 1999.

[27] I. Harris and D.-L. Nguyen. Orthogonality sampling method for the electromagnetic inverse scattering problem. *SIAM J. Sci. Comput.*, 42:B72–B737, 2020.

[28] C. Alves, R. Kress, and P. Serranho. Iterative and range test methods for an inverse source problem for acoustic waves. *Inverse Problems*, 25:055005, 2009.

[29] R. Kress and W. Rundell. Reconstruction of extended sources for the Helmholtzholtz equation. *Inverse Problems*, 29:035005, 2013.

[30] I. Catapano, L. Crocco, M. D'Urso, and T. Isernia. 3D microwave imaging via preliminary support reconstruction: testing on the Fresnel 2008 database. *Inverse Problems*, 25:024002, 2009.

[31] P. C. Chaumet and K. Belkebir. Three-dimensional reconstruction from real data using a conjugate gradient coupled dipole method. *Inverse Problems*, 25:024003, 2009.

[32] J. DeZaeytijd and A. Franchois. 3D quantitative microwave imaging from measured data with multiplicative smoothing and value picking regularization. *Inverse Problems*, 25:024004, 2009.

[33] D. Colton and A. Kirsch. A simple method for solving inverse scattering problems in the resonance region. *Inverse Problems*, 12:383–393, 1996.

[34] A. Kirsch. An integral equation for the scattering problem for an anisotropic medium and the Factorization method. In *8th int. workshop on mathematical methods in scattering theory and biomedical engineering*, 2007.

[35] S. Antholzer, M. Haltmeier, and J. Schwab. Deep learning for photoacoustic tomography from sparse data. *Inverse Probl. Sci. Eng.*, 27:987–1005, 2017.

[36] S. J. Hamilton and A. Hauptmann. Deep d-bar: Real-time electrical impedance tomography imaging with deep neural networks. *IEEE Trans Med Imaging*, 37:2367–2377, 2018.

[37] K. H. Jin, M. T. McCann, E. Froustey, and M. Unser. Deep convolutional neural network for inverse problems in imaging. *IEEE Trans. Image Process.*, 26:4509–4522, 2017.

[38] Y. Khoo and L. Ying. Switchnet: A neural network model for forward and inverse scattering problems. *SIAM J. Sci. Comput.*, 41:A3182–A3201, 2019.

[39] L. Li, L. G. Wang, F. L. Teixeira, C. Liu, A. Nehorai, and T. J. Cui. Deepnis: Deep neural network for nonlinear electromagnetic inverse scattering. *IEEE Trans. Antennas Propag.*, 67:1819–1825, 2019.

[40] J. Xiao, J. Li, Y. Chen, F. Han, and Q. H. Liu. Fast electromagnetic inversion of inhomogeneous scatterers embedded in layered media by born approximation and 3-d u-net. *IEEE Geosci. Remote. Sens. Lett.*, 17:1677–1681, 2020.

[41] S. Kang and M. Lambert. Structure analysis of direct sampling method in 3d electromagnetic inverse problem: near- and far-field configuration. *Inverse Problems*, 37: 075002, 2021.

[42] D. Colton and R. Kress. *Inverse Acoustic and Electromagnetic Scattering Theory*. Springer, New York, 3rd edition, 2013.

[43] K. Ito, K. Ramdani, and M. Tucsnak. A time reversal based algorithm for solving initial data inverse problems. *Discrete Contin. Dyn. Syst. Ser. S*, 4:641–652, 2010.

[44] K. Ito, B. Jin, and J. Zou. A direct sampling method for inverse electromagnetic medium scattering. *Inverse Problems*, 29:095018, 2013.

[45] D.-L. Nguyen. Direct and inverse electromagnetic scattering problems for bi-anisotropic media. *Inverse Problems*, 35:124001, 2019.

[46] F. Chollet. Deep learning with depthwise separable convolutions. *arXiv:1610.02357*, 2016.

[47] N. Ahn, B. Kang, and K.-A. Sohn. Fast, accurate, and lightweight super-resolution with cascading residual network. *arXiv:1803.08664*, 2018.

[48] J. Redmon and A. Farhadi. Yolov3: An incremental improvement. *arXiv:1804.02767*, 2018.

[49] M. Sandler, A. Howard, M. Zhu, A. Zhmoginov, and L.-C. Chen. Mobilenetv2: Inverted residuals and linear bottlenecks. *arXiv:1801.04381*, 2019.

[50] A. Lechleiter and D.-L. Nguyen. A trigonometric Galerkin method for volume integral equations arising in tm grating scattering. *Adv. Comput. Math.*, 40:1–25, 2014.

[51] P. Monk. *Finite Element Methods for Maxwell's Equations*. Oxford, 2003.

[52] A. Kirsch. The factorization method for Maxwell's equations. *Inverse Problems*, 20: 117–134, 2004.

[53] F. Cakoni, D. Colton, and H. Haddar. *Inverse Scattering Theory and Transmission Eigenvalues*. SIAM, 2016.

[54] H. Haddar. Analysis of some qualitative methods for inverse electromagnetic scattering problems. In *Bermudez de Castro A., Valli A. (eds) Computational Electromagnetism. Lecture Notes in Mathematics, vol 2148*, pages 191–240. Springer, Cham, 2014.

[55] D. Colton and A. Kirsch. A simple method for solving inverse scattering problems in the resonance region. *Inverse Problems*, 12:383, 1996.

[56] A. Kirsch. An integral equation approach and the interior transmission problem for Maxwell's equations. *Inverse Probl. Imaging*, 1:159–180, 2007.

[57] A. Kirsch and N.I. Grinberg. *The Factorization Method for Inverse Problems*. Oxford Lecture Series in Mathematics and its Applications 36. Oxford University Press, 2008.

[58] J. M. Geffrin and P. Saboroux. Continuing with the Fresnel database: experimental set-up and improvements in 3D scattering measurements. *Inverse Problems*, 25:024001, 2009.

[59] F. Cakoni and D. Colton. *Qualitative Methods in Inverse Scattering Theory. An Introduction.* Springer, Berlin, 2006.